Applied Catalysis B: Environmental 343 (2024) 123563

Contents lists available at ScienceDirect

Applied Catalysis B: Environmental

journal homepage: www.elsevier.com/locate/apcatb

Highly efficient water-splitting electrodes with stable operation at 3 A cm^{-2} in alkaline media through molecular linker assembly-induced all-in-one structured NiMo and NiFe electrocatalysts

Youhyun Son [a], Jeongmin Mo [a], Euiju Yong [a], Jeongyeon Ahn [a], Gyuchan Kim [b], Wonyoung Lee [b], Cheong Hoon Kwon [c], Hyun Ju [d], Seung Woo Lee [d], Byung-Hyun Kim [e,f,*], Myeongjin Kim [b,**], Jinhan Cho [a,g,h,***]

[a] Department of Chemical and Biological Engineering, Korea University, 145 Anam-ro, Seongbuk-gu, Seoul 02841, Republic of Korea
[b] Department of Hydrogen & Renewable Energy, Kyungpook National University, 80 Daehakro, Bukgu, Daegu 41566, Republic of Korea
[c] Department of Energy Resources and Chemical Engineering, Kangwon National University, Samcheok 25913, Republic of Korea
[d] The George W. Woodruff School of Mechanical Engineering Georgia Institute of Technology, Atlanta, GA 30332, USA
[e] Department of Chemical and Molecular Engineering, Hanyang University ERICA, 55 Hanyangdaehak-ro, Sangnok-gu, Ansan-si, Gyeonggi-do 15588, Republic of Korea
[f] Department of Applied Chemistry, Center for Bionano Intelligence Education and Research, Hanyang University ERICA, 55 Hanyangdaehak-ro, Sangnok-gu, Ansan-si, Gyeonggi-do 15588, Republic of Korea
[g] KU-KIST Graduate School of Converging Science and Technology, Korea University, 145 Anam-ro, Seongbuk-gu, Seoul 02841, Republic of Korea
[h] Soft Hybrid Materials Research Center, Advanced Materials Research Division, Korea Institute of Science and Technology (KIST), Seoul 02792, Republic of Korea

ARTICLE INFO

Keywords:
Water-splitting
Carbon nanotube
Binary nonnoble metal

ABSTRACT

Developing nonnoble electrocatalyst-based water-splitting electrodes with high operational stability and low overpotentials is one of the most critical challenges in commercially available water-splitting reactions. In this study, we present water-splitting textile electrodes enabling remarkably low overpotentials and high stable operation. We first assembled conductive multi-walled-carbon-nanotubes (MWCNTs) with amine molecule-based linkers onto cotton textiles and subsequently electrodeposited Ni onto the MWCNT-incorporated textile. For the preparation of hydrogen evolution reaction (HER) and oxygen evolution reaction (OER) electrodes, NiMo and NiFe were further electrodeposited onto the Ni-electrodeposited textile electrode, respectively. These electrodes exhibited considerably low overpotentials in alkaline media (8 mV at 10 mA cm^{-2} for HER and 189 mV at 50 mA cm^{-2} for OER). Furthermore, the full-cell electrodes preserved a low cell voltage of 2.01 V at an unprecedentedly high current density of 3000 mA cm^{-2} for a prolonged duration (> at least 1000 h).

1. Introduction

Serious concerns about global warming, environmental pollution, and energy crisis have led to a strong demand for renewable/clean energy sources and processes that can completely replace conventional fossil fuels, which emit large amounts of carbon dioxide. Among various energy sources and processes, hydrogen (H_2) gas produced from an electrolytic water-splitting reaction is considered one of the most promising energy sources and carriers due to its environmental friendliness and high energy density [1–6]. However, its production efficiency is severely restricted by the short lifespan and low catalytic performances of hydrogen evolution reaction (HER) and oxygen evolution reaction (OER) electrodes used in water-splitting cells. Although noble metal catalysts such as Pt, Ru, and Ir exhibit high water-splitting efficiency, their scarcity and high cost present a significant obstacle to the improvement of commercially available electrolytic water-splitting electrodes (EWSE) [7,8]. Moreover, despite the use of these noble metal catalysts, the electrodes are still subject to the issue of short-term operation stability due to unfavorable interfacial interactions between catalysts and a host electrode, as well as between neighboring catalysts.

* Corresponding author at: Department of Chemical and Molecular Engineering, Hanyang University ERICA, 55 Hanyangdaehak-ro, Sangnok-gu, Ansan-si, Gyeonggi-do 15588, Republic of Korea.
** Corresponding author.
*** Corresponding author at: Department of Chemical and Biological Engineering, Korea University, 145 Anam-ro, Seongbuk-gu, Seoul 02841, Republic of Korea.
E-mail addresses: bhkim00@hanyang.ac.kr (B.-H. Kim), myeongjinkim@knu.ac.kr (M. Kim), jinhan71@korea.ac.kr (J. Cho).

https://doi.org/10.1016/j.apcatb.2023.123563
Received 20 September 2023; Received in revised form 17 November 2023; Accepted 24 November 2023
Available online 29 November 2023
0926-3373/© 2023 The Author(s). Published by Elsevier B.V. This is an open access article under the CC BY-NC-ND license (http://creativecommons.org/licenses/by-nc-nd/4.0/).

To address these issues, substantial research has been dedicated to developing high-performance electrodes with low overpotentials and long-term durability using a variety of nonnoble metal electrocatalysts, such as 3*d* oxides [9–11], phosphates [12–16], nitrides [17,18], sulfides [19,20], and perovskite, which have been explored in alkaline environments. For instance, depositing electrocatalytic Ni-based alloys onto 3D-structured current collectors (*i.e.*, porous carbon cloth or Ni foam) *via* chemical reduction or hydrothermal methods has resulted in electrodes exhibiting low overpotentials of 20–40 mV at 10 mA cm^{-2} for HER [11,12,18,21] and 220–300 mV at 50 mA cm^{-2} for OER [14–17,22,23] in KOH solution, respectively. However, ensuring operational stability and water-splitting efficiency at higher current density has proven challenging, primarily due to nonuniform deposition and poor interfacial interactions of electrocatalysts across all regions of 3D-structured current collectors, ranging from the exterior to the interior.

A cell voltage required for commercially available full-cell-devices comprised of HER and OER electrodes to deliver current densities of 300–400 mA cm^{-2} is approximately 1.7–2.4 V [6]. On the other hand, to sustainably produce larger amounts of hydrogen gas, the electrodes need to enable stable operation at higher current densities (> 400 mA cm^{-2}) for a long time. However, in most research works reported to date, the operational stability tests have been mainly conducted under current

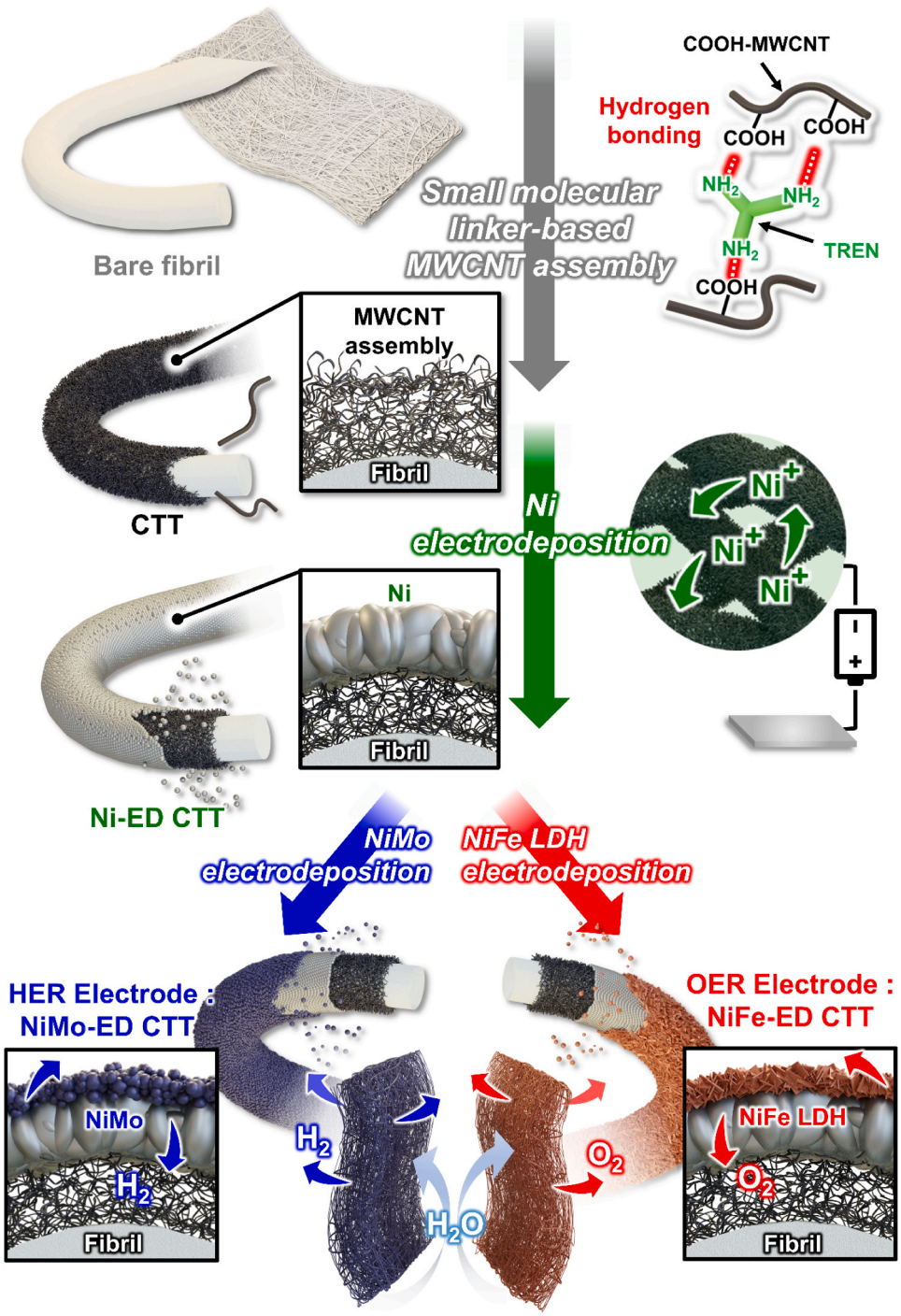

Scheme 1. Schematic representation of the fabrication of water-splitting electrodes using electrodeposition induced by MWCNT/small molecular linker assembly. The structures of assembled electrodes were ideally represented.

densities lower than 400 mA cm^{-2}, which also have much difficulty in securing the long-term operation time of above 1000 h [24,25]. Particularly, it is important to note that a significant increase in amounts of H_2 and O_2 gas bubbles generated from water-splitting cells at high current density has a strong impact on the operational stability of EWSEs because electrocatalysts are weakly adsorbed onto the host electrodes through conventional slurry casting, chemical reduction of electrocatalytic metal ions, or hydrothermal method. These phenomena are applicable to nearly all water-splitting electrodes, irrespective of whether they consist of noble or nonnoble metal catalysts. Therefore, to achieve long-term operation of commercially available EWSEs with high water-splitting efficiency even at an extremely high current density (> 2000 mA cm^{-2}), it is highly desirable to establish all-in-one structured interfaces within the electrodes, comprising the substrate, conductive components, and highly efficient electrocatalysts, through favorable interfacial interactions without any harsh chemical or high-temperature treatment [9–26]. Moreover, electrocatalysts should be conformally assembled across all regions of 3D-structured current collectors to maximize the electrocatalytic surface area of water-splitting HER and OER electrodes.

Herein, we present the development of high-performance robust HER and OER electrodes with remarkably low overpotentials (8 mV at 10 mA cm^{-2} for HER and 189 mV at 50 mA cm^{-2} for OER in 1 M KOH media at room temperature) and exceptional operation stability even under exceptionally high current density of 3000 mA cm^{-2}. These electrodes could be fabricated by employing molecular linker-mediated carbon nanotube assembly-induced nonnoble binary metal electrodeposition without aids of noble metals and/or thermal treatments, as illustrated in Scheme 1. Particularly, considering that a harsh process such as high-temperature carbonization renders various textiles such as cotton, polyester, or nylon extremely vulnerable to external stimuli possibly induced by bubble pressure, it should be noted that our approach is widely applicable to a variety of textiles for the preparation of 3D current collectors. Additionally, our electrodes demonstrated a substantial active surface area, facilitated by the highly nanoprotuberant structure in the case of the HER electrode and the nanowrinkled structure for the OER electrode. Moreover, the formation of microporous structure (by numerous fibrils) within textile further could enhance the electrocatalytic performance of electrodes.

Specifically, small molecular linker-mediated carbon nanotube assembly shown in our approach, has proven to be instrumental in achieving several key outcomes. One crucial aspect is the conformal deposition of a conductive seed layer onto the textile fibrils. This process further expands the surface area of the pristine textile without compromising its mechanical properties. Additionally, it effectively minimizes contact resistances between adjacent carbon nanotubes, leading to improved conductivity within the textile material. It is worth mentioning that the electrical conductivity of small molecular linker-mediated carbon nanotube assembled film is much higher than those of conventional carbon nanotube films. Additional notable advantage of our approach is that the enhanced surface area achieved through the carbon nanotube assembly has a significant impact on enlarging the active surface area of the resulting water-splitting electrodes. This improvement is a critical factor in enhanced performance and efficiency of the electrodes during the water-splitting process. That is, our approach's utilization of small molecular linker-mediated carbon nanotube assembly is pivotal in expanding the textile's surface area, improving conductivity, and providing a strong foundation for the water-splitting electrodes. In addition to providing a significantly expanded active surface area, the utilization of electroplated Ni alloy catalysts, namely NiMo for HER and NiFe for OER, offered more facile reaction pathways and a more robust mechanical structure compared to conventional Ni and hydrothermal-induced Ni alloys, respectively. This unique combination yielded unprecedently low overpotentials, surpassing what could typically be achieved with Pt and Ir (or Ru) electrocatalyst-based electrodes, as well as previously reported Ni alloy-based electrodes.

For this goal, we used carboxylic acid−functionalized multi-walled-carbon nanotubes (COOH-MWCNTs) assembled with amine (NH_2)-functionalized molecular linkers (tris(2-aminoethyl) amine, TREN) onto cotton textile utilizing hydrogen-bonding interactions. The use of these molecular linkers with an exceptionally small molecular weight ($M_w \sim$ 146 g mol^{-1}) onto textile significantly reduced the interfacial contact resistances between neighboring COOH-MWCNTs and established direct bridging between adjacent COOH-MWCNTs as well as between pristine textile and COOH-MWCNTs. Additionally, the surface area of MWCNT/TREN-assembled textile was 1.6 times larger than bare textile. For the preparation of the host electrodes with high conductivity comparable to bulk metal, a Ni layer was electrodeposited onto the outermost NH_2-functionalized TREN-coated layer of COOH-MWCNT/TREN-assembled textile. Thereafter, either Ni-Mo or Ni-Fe layer was subsequently electrodeposited onto the Ni electroplated MWCNT-coated textile electrodes, respectively. In this case, the Ni-Mo layer was prepared for the HER electrode and the Ni-Fe layer was developed for the OER electrode. These steps resulted in the formation of nanoprotuberant-structured NiMo and nanowrinkled NiFe-based textile electrodes, which possessed large active surface areas and low skeletal mass densities of approximately 1.62 g cm^{-3} (compared to the mass density of bulk nickel, including Ni foam or Ni felt, which is approximately 8.91 g cm^{-3}). The interfaces within the formed HER and OER electrodes were robustly bridged through hydrogen, covalent, and metallic bonding interactions. Additionally, the numerous fibrils constituting the complex textile underwent a complete transformation into electrocatalytic fibrils with a significant surface area due to the inherent nanostructure. Consequently, the HER and OER textile-based electrodes exhibited low overpotentials of 8 mV at 10 mA cm^{-2} and 189 mV at 50 mA cm^{-2}, respectively. Furthermore, when integrated into a full-cell electrolyzer water-splitting system (EWSE), comprising these electrodes, the system demonstrated highly stable operation for at least 1000 h, delivering a cell voltage as low as 2 V even when subjected to an extremely high current density of up to 3000 mA cm^{-2}, surpassing the performance of previous EWSEs. The exceptional water-splitting capabilities of these textile electrodes were corroborated through *in-situ* X-ray analysis, operando Raman analysis, and density functional theory (DFT) calculations. Overall, our approach presents a promising foundation for the design and development of highly efficient EWSEs.

2. Experimental section

2.1. Materials

All chemical reagents used in our study were purchased from Sigma-Aldrich and handled without further purification. Cotton textiles (4.5 cm × 4 cm × 790 μm) were purchased from Cottonday (Republic of Korea). The diameter of the fibers which compose the textile is about 14.6 μm. Pristine MWCNTs exhibiting a diameter of 7–9 nm, length of 10–50 μm, and purity greater than 80%, obtained from Nanosolution Co. LTD., were subjected to acidic treatment using a mixture of HNO_3/H_2SO_4 at 75 °C. The resulting COOH-MWCNTs were repeatedly washed using a centrifuge and vacuum filter process to eliminate byproducts and acidic residues. Finally, ethanol was used as a solvent to redisperse the COOH-MWCNTs.

2.2. Preparation of textile electrodes

To fabricate a (COOH-MWCNT/TREN)$_n$ multilayer-coated textile (CTT) using a layer-by-layer (LbL) assembly, both COOH-MWCNTs and TREN were dispersed using ethanol (2 mg mL^{-1}). Initially, a cotton textile with cellulose fibrils with numerous hydroxyl (OH)-functional groups was immersed in poly(ethylene imine) (PEI)-dissolved ethanol solution (2 mg mL^{-1}) for 18 h, which converted OH-functional cotton textile into NH_2-functional textile. After this surface treatment, the

textile was dipped into COOH-MWCNT solution for 15 min to induce hydrogen bonding-based adsorption. The COOH-MWCNT-coated textile was then washed several times using pure ethanol to clear weakly bonded COOH-MWCNTs away. Afterwards, the textile with adsorbed COOH-MWCNTs was immersed in an NH_2-functionalized TREN solution for 15 min, again, and then a washing procedure was repeated. These dipping and washing procedures were repeated to get the desired number of bilayers.

To prepare the Ni-electrodeposited $(COOH\text{-}MWCNT/TREN)_{20}$-coated textile (Ni-ED CTT), a Ni plate and the as-prepared CTT were connected to an electroplating circuit as an anode and cathode, respectively. These electrodes were then dipped into a Watt bath containing 45 g L^{-1} $NiCl_2$, 240 g L^{-1} $NiSO_4$, and 30 g L^{-1} H_3BO_3 [27]. The Ni electrodeposition step was conducted at 350 mA cm^{-2} for 5 min with an Ivium-n-Stat workstation (Ivium Technologies). After the electrodeposition process, the formed Ni-ED CTT was washed several times with DI water, and then dried at room temperature for 8 h under vacuum conditions. In this case, the Ni loading amount was estimated to be approximately 61.4 mg cm^{-1}.

MWCNT-free Ni-ED textile was fabricated using the same electrodeposition method as Ni-ED CTT. However, before electrodeposition, both sides of cotton textile were coated with Au (150 s sputtering at the current of 30 mA) using ion sputtering equipment (Hitachi, MC1000). This process produced a conductive textile with a sheet resistance of about 2.0×10^3 Ω sq^{-1}.

A NiMo layer was electrodeposited onto the Ni-ED CTT electrode in the electrolyte solution containing 80 g L^{-1} $NiSO_4$, 50 g L^{-1} Na_2MoO_4, 90 g L^{-1} $Na_3C_6H_5O_7$, deionized (DI) water, and an excess amount of NH_4OH. In this case, the pH of electrolyte solution was adjusted to 10.5 [28]. The NiMo electrodeposition was conducted at 150 mA cm^{-2} for 7 min using an Ivium-n-Stat workstation (Ivium Technologies). When the electrodeposition process was finished, the NiMo-ED CTT (*i.e.*, NiMo/Ni-ED CTT) was cleaned with DI water several times and dried at room temperature for 8 h under vacuum conditions (NiMo loading amount: 4.5 mg cm^{-1}).

A layer of NiFe layered double hydroxide (LDH) was electrodeposited onto the Ni-ED CTT electrode in electrolyte solution containing 5 mM $Ni(NO_3)_2{\cdot}6\,H_2O$, 1 mM $Fe(NO_3)_3{\cdot}9\,H_2O$, and DI water [29]. Then, the process of NiFe LDH electrodeposition was conducted at 10 mA cm^{-2} for 60 min using Ivium-n-Stat workstation (Ivium Technologies). When the electrodeposition process was finished, the NiFe-ED CTT (*i.e.*, NiFe LDH/Ni-ED CTT) was cleaned with DI water several times and dried at room temperature for 8 h under vacuum condition (NiFe loading amount: 4.3 mg cm^{-1}).

2.3. Characterization

Fourier-transform infrared spectroscopy (FTIR) analysis was conducted utilizing a Cary 600 spectrometer (Agilent Technology). To obtain the spectra of COOH-MWCNT and TREN, an attenuated total reflection (ATR) mode, operating at a resolution of 2 cm^{-1} was applied. An advanced grazing angle (AGA) mode operating at a resolution of 4 cm^{-1}, was used to obtain the spectra of multilayers. The obtained data were baseline-corrected and smoothed using spectral analysis software (OMNIC, Nicolet). The UV–vis spectra of $(COOH\text{-}MWCNT/TREN)_n$ films on quartz glasses were acquired with a Lambda 365 (Perkin Elmer) spectrophotometer, within a wavelength from 200 nm to 1000 nm. A QCM (QCM 200, SRS) was utilized to quantitively identify the mass change (Δm) of each layer by measuring the frequency change (ΔF).

Water contact angles and skeletal density were measured using a Phoenix 300 (S.E.O. Co., Ltd.) and mercury intrusion porosimetry (AutoPore V 9600, Micromeritics). The Brunauer–Emmett–Teller (BET) specific surface areas of bare textile, CTT, and Ni-ED CTT were obtained *via* N_2 adsorption at 77 K (Autosorb-iQ and Quadrasorb SI). SmartLab (Rigaku) with Cu Kα radiation source was used to examine X-ray diffraction (XRD) patterns.

The surface morphology, energy-dispersive X-ray spectroscopy (EDS) mapping images, crystal structures, and chemical compositions of electrodes were studied using the field-emission scanning electron microscopy (FE-SEM) (Quanta 250 FEG, FEI), EDS, high-resolution transmission electron microscopy (HR-TEM) (JEM-F200 (TFEG) equipment (JEOL Ltd.)), and X-ray photoelectron spectroscopy (XPS) (ULVAC-PHI). XPS spectra were charge-corrected using C 1 s peak assigned to C-C/C-H binding energy (284.8 eV).

X-ray absorption spectroscopy (XAS) measurements were performed at the BL7D beamline in the Pohang Light Source (PLS), which operated in the top-up mode with a ring current of 300 mA at 3.0 GeV. The incident beam underwent collimation by a Ru-coated mirror at 2.8 mrad and monochromatization using a channel-cut Si (1 1 1) monochromator. Processing of the acquired extended X-ray absorption fine structure (EXAFS) data followed standard procedures, employing the ATHENA module within the IFEFFIT software packages. To obtain the EXAFS spectra, the post-edge background was subtracted from the overall absorption, followed by normalization with respect to the edge-jump step. Subsequently, the $\chi(k)$ data in k-space underwent Fourier transformation to real (R) space, utilizing a Hanning window to separate the EXAFS contributions from different coordination shells.

2.4. Electrochemical characterization

Linear sweep voltammetry (LSV), Cyclic voltammetry (CV), and electrochemical impedance spectroscopy (EIS) measurements were conducted using an Ivium-n-Stat electrochemical workstation. A Pt mesh and reversible hydrogen electrode (RHE) were respectively used as counter and reference electrodes in the 1 M KOH electrolyte for measurements in a three-electrode cell system. The HER and OER catalytic activities were measured by LSV and CV, respectively, at scan rates of 2 mV s^{-1} with *iR* compensation. All current densities reported were measured based on the geometric surface area of the electrodes. The EIS curves were obtained with a biased working electrode at frequencies ranging from 100 kHz to 0.01 Hz and potentials of − 0.1 V (*vs*. RHE) for the HER and 1.5 V (*vs*. RHE) for the OER. The size of the electrodes was fixed at 0.5×0.5 cm^2.

Operando Raman spectra were obtained *via* an instrument (DXR2xi, Thermo, USA) with a 514 nm argon laser (power: 1 mW) during LSV experiments. A home-made electrochemical configuration, consisting of a prepared catalyst as a working electrode, Pt wire as a counter electrode, and Ag/AgCl (KCl Sat.) as a reference electrode was used. The amount of Ni, Mo, and Fe ions dissolved in the electrolyte was measured using inductively coupled plasma mass spectrometry (ICP-MS, Agilent Technologies 7700) after the full cell test.

3. Results and discussion

3.1. MWCNT assembly-driven conductive textile

For the preparation of MWCNT assembly-driven EWSE, we first transformed pristine MWCNTs to COOH-MWCNTs using an HNO_3/H_2SO_4 oxidative method (**Fig. S1**) [30,31]. We then sequentially assembled these COOH-MWCNTs with NH_2-functionalized TREN molecular linkers using hydrogen-bonding interaction in ethanol to deposit $(COOH\text{-}MWCNT/TREN)_n$ multilayers onto substrates. FTIR spectra of COOH-MWCNTs and TREN revealed absorption peaks originating from the C═O stretching vibration of COOH groups around 1720 cm^{-1} and N-H bending vibration of NH_2 groups around 1610 cm^{-1}, respectively (**Fig. S2**) [32,33]. With increasing the bilayer number (n) of $(COOH\text{-}MWCNT/TREN)_n$ from 0.5 to 2, the absorption peak intensities of the COOH and NH_2 groups were alternately intensified (Fig. 1**a**).

Furthermore, as the bilayer number (n) increased from 5 to 20, the total film thicknesses of the $(COOH\text{-}MWCNT/TREN)_n$ multilayers almost linearly increased from 135 (for $n = 5$) to 564 nm ($n = 20$), which was also confirmed by cross-sectional FE-SEM images and UV–vis

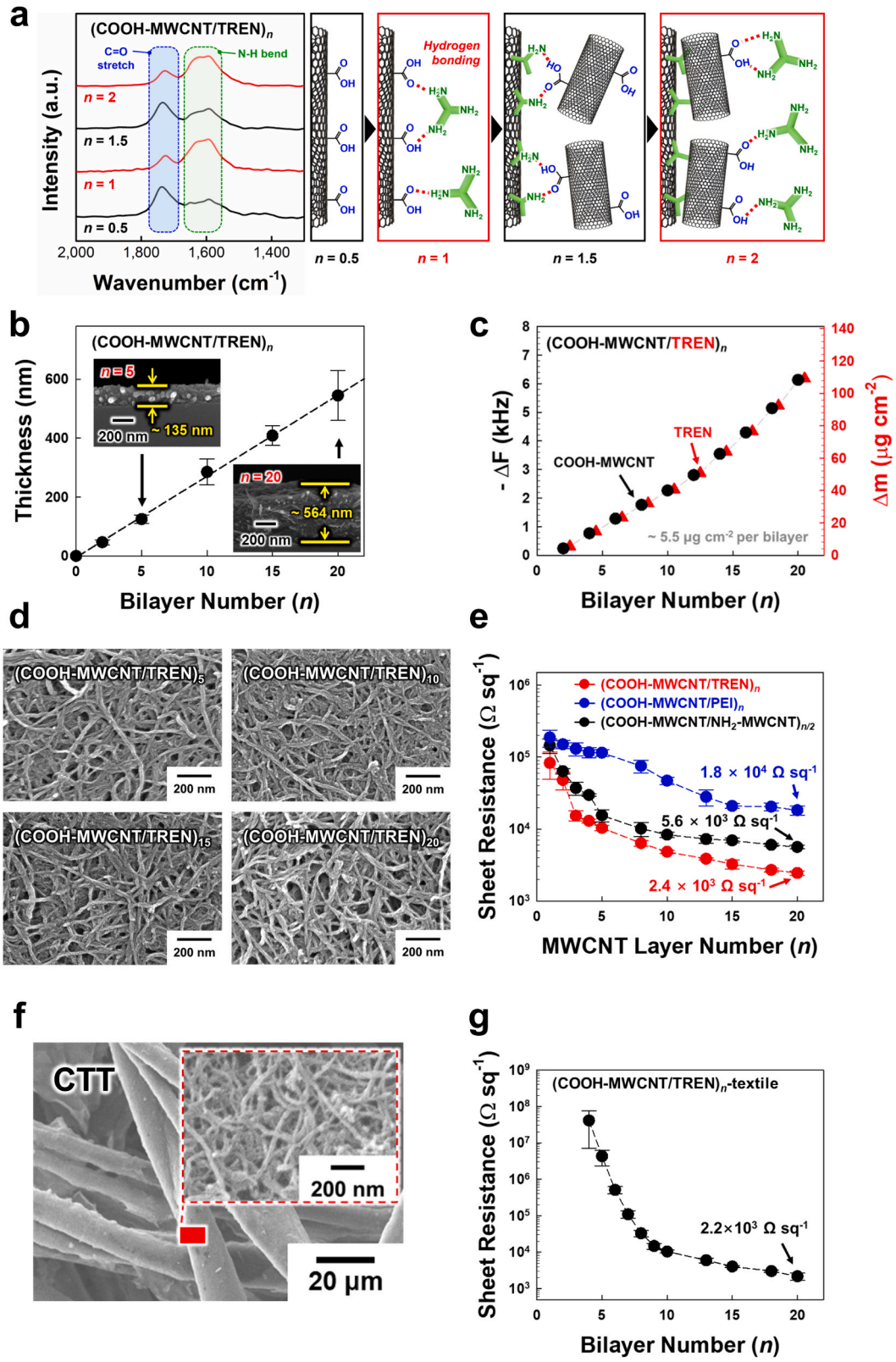

Fig. 1. Preparation of the COOH-MWCNT/TREN multi-layer coated textile. a) FTIR spectra of a (COOH-MWCNT/TREN)$_n$ multilayer as a function of the bilayer number (n) and corresponding illustration of the cohesive mechanism. b) Film thickness of (COOH-MWCNT/TREN)$_n$ multilayers on Si wafers as a function of the bilayer number (n) gauged by the cross-sectional FE-SEM images (inset). c) QCM measurements of change in frequency ($-\Delta F$, left axis) and mass ($-\Delta m$, right axis) of (COOH-MWCNT/TREN)$_n$ multilayers with increasing bilayer number. d) Planar FE-SEM images of the (COOH-MWCNT/TREN)$_n$ multilayers at the bilayer number of 5, 10, 15, and 20. e) Sheet resistance of the (COOH-MWCNT/linker)$_n$ multilayers (linker: TREN, PEI, NH_2-MWCNT) as the MWCNT layer number increased from 1 to 20. f) Planar FE-SEM images of the CTT at varying degrees of magnification. g) Electrical properties of the CTT with increasing bilayer number (n).

spectroscopy (Fig. 1**b** and **Fig. S3**). The mass changes per bilayer were calculated using quartz crystal microbalance (QCM) and estimated to be approximately 5.5 μg·cm^{-2} ($\Delta F \sim 309$ Hz) (Fig. 1**c and Supplementary detailed experimental procedures**). Another significant benefit of these COOH-MWCNT/TREN films, with their controllable film thickness, is that they maintain a highly uniform nanoporous structure and hydrophilic surface, even as the total multilayer thickness continuously increases with the bilayer number (Fig. 1**d and** Fig. S4). These uniformity and hydrophilic surface are noteworthy because they enable infiltration of hydrophilic ions, such as nonnoble metal ions for electrodeposition, into the (COOH-MWCNT/TREN)$_n$ films, unlike pristine MWCNT films, which have hydrophobic properties (**Fig. S4**). Such properties are critical in achieving uniform catalytic metal electrodeposition onto the films.

In addition, our assembly approach, which employs an extremely small molecular linker, provides a significant advantage by minimizing the electrical resistance between neighboring COOH-MWCNTs. This is in stark contrast to the electrical resistance observed in conventional MWCNT multilayers that use NH_2-functionalized MWCNTs (*i.e.*, NH_2-MWCNTs) or insulating NH_2-functionalized polymeric linkers such as PEI (Fig. 1**e**). Previous studies have shown that the LbL-assembled TREN molecule layer has an extremely thin thickness of approximately 5.6 Å, which does not impede electron transfer [34]. With an aid of these molecular linkers, the sheet resistance of multilayers was reduced from 8.3×10^4 to 2.4×10^3 Ω sq^{-1} when the bilayer number (n) of multilayers onto a nonporous, flat Si wafer was increased from 1 to 20. This low electrical resistance value of 2.4×10^3 Ω sq^{-1} is suitable for Ni electrodeposition.

Based on these electrical properties and adsorption behaviors of (COOH-MWCNT/TREN)$_n$, the multilayers were deposited onto the 3D-structued porous textile with numerous OH group-functionalized fibrils, referred to as COOH-MWCNT and TREN-coated textile, CTT. The NH_2 groups of the linkers directly bridged the interfaces between fibrils within cotton textile and COOH-MWCNTs, as well as between neighboring COOH-MWCNTs through hydrogen-bonding interactions. As a result, the COOH-MWCNT multilayers were uniformly covered the entire surface from the exterior to the interior of the textile (Fig. 1f and **Fig. S5**). Additionally, when the bilayer number (n) of (COOH-MWCNT/TREN)$_n$ multilayers was accumulated up to 20, the sheet resistance of the (COOH-MWCNT/TREN)$_n$ multilayer-coated textile was reduced to 2.2×10^3 Ω sq^{-1}, which was nearly identical to that of the (COOH-MWCNT/TREN)$_{20}$ multilayer-coated Si wafer (Fig. 1g).

3.2. Ni-electrodeposited textile using MWCNT assembly

Based on this conductive textile, we further attempted to create a porous host electrode that functions as a conductive support with bulk metal-like electrical conductivity for water-splitting electrocatalysts. To this end, we electrodeposited Ni metal over the electrically conductive textile with a sheet resistance of 2.2×10^3 Ω sq^{-1}, resulting in a metallic substrate with a highly porous textile structure and an exceptionally low sheet resistance of approximately 0.06 Ω sq^{-1} (Fig. 2a,b). It is worth noting that this conformal electrodeposition was not easily achievable using the aforementioned COOH-MWCNT/NH_2-MWCNT or COOH-MWCNT/PEI multilayers due to their relatively high electrical resistance (see Fig. 1**e**). Additionally, although 61.4 mg cm^{-2} of Ni was electrodeposited, the skeletal mass density of Ni-electrodeposited (COOH-MWCNT/TREN)$_{20}$ multilayer-coated textile (*i.e.*, Ni-ED CTT) was estimated to be 1.58 g cm^{-3} (the total mass density of Ni-ED CTT ~ 0.93 g cm^{-3}), which was much lower than that of bulk nickel (mass density ~ 8.91 g cm^{-3}) including Ni foam or Ni felt.

The chemical structure of Ni-electrodeposited (COOH-MWCNT/TREN)$_{20}$ multilayer-coated textile (*i.e.*, Ni-ED CTT) was studied using XPS. The Ni 2p data obtained from Ni-ED CTT exhibited strong peak intensity originating from metallic Ni (*i.e.*, Ni^0 $2p_{3/2}$ at 853.1 eV and Ni^0 $2p_{3/2}$ at 870.4 eV) and $Ni(OH)_2$ (Ni^{2+} $2p_{3/2}$ at 856.3 eV and Ni^{2+} $2p_{1/2}$ at 874.4 eV) (Fig. 2c) [35–37]. The presence of $Ni(OH)_2$ could also be confirmed from the O 1 s peak observed at 531.3 eV (**Fig. S6**) [37–39]. Additionally, XRD analysis revealed that the crystalline structure of Ni-ED CTT layer was composed of face-centered cubic (fcc) Ni and α-Ni$(OH)_2$ (Fig. 2d). Despite this electrodeposition of Ni-ED CTT, it still preserved the high mechanical flexibility of the pristine cotton textile. Specifically, the electrical conductivity of Ni-ED CTT after 10,000 bending cycles (with a bending radius (R) of approximately ~ 0.2 cm) maintained about 98.4% of its initial electrical conductivity (Fig. 2e). These results demonstrate that our approach for Ni-ED CTT can have both the electrical conductivity comparable to bulk metal and the high mechanical flexibility of the bare cotton textile.

Another notable feature of Ni-ED CTT is its significantly large surface area, achieved through a highly nanoprotuberant structure. It is important to note that this nanostructure-induced large surface area of the electrodeposited Ni layer can also have a significant effect on the surface area of the subsequently electrodeposited electrocatalysts (*i.e.*, NiMo layer for HER and NiFe LDH layer for OER). First, the large surface area of Ni-ED CTT was confirmed by BET analysis (Fig. 2f). In this case, the surface area of Ni-ED textile (about 3.6 m^2 g^{-1}) was larger than that of the COOH-MWCNT multilayer-coated textile (about 2.7 m^2 g^{-1}) without Ni-electrodeposition, and that of the bare textile (about 1.7 m^2 g^{-1}) due to the prominent nanostructure of Ni layer created during Ni electrodeposition (as shown in Fig. 2b). To further compare the surface area of Ni-ED CTT with that of other Ni-based 3D porous current collectors, we estimated the electrochemically active surface area (ECSA) using the double-layer capacitance (C_{dl}) (Fig. 2g and Fig. S7). Based on the scan rate-dependent CV in 1 M KOH (Fig. S7) and the linear fitting (Fig. 2g), the C_{dl} of Ni-ED CTT was calculated to be approximately 134 mF cm^{-2}. This value was about 30 and 200 times larger than that of conventional Ni-electrodeposited carbon cloth (about 5.0 mF cm^{-2}) and commercially available Ni foam (about 0.6 mF cm^{-2}), respectively. It should also be noted that the ECSA of Ni-ED CTT was about 2 times larger than that (about 62.8 mF cm^{-2}) of MWCNT-free Ni-ED textile (see **Experimental section**).

For a better understanding of the effect of MWCNT sublayers on the surface area and chemical properties of the host electrode, the Ni layer was electrodeposited onto the MWCNT-coated Si wafer (sheet resistance of ~2000 Ω sq^{-1}), the MWCNT-free Au/Si wafer (sheet resistance of ~3 Ω sq^{-1}), and the bare Ni plate (sheet resistance of < 0.01 Ω sq^{-1}), respectively. Then, water contact angle measurements were performed on these three different samples. We found that the water contact angle of Ni-electrodeposited (COOH-MWCNT/TREN)$_{20}$/Si wafer was lower than that of the Ni-electrodeposited MWCNT-free Au/Si wafer and bare Ni plate. Although the outermost layers of all samples were composed of Ni with almost the same chemical properties (**Fig. S8**), their water contact angles strongly depended on the degree of surface roughness, which is closely related to the surface area described with Wenzel's model as follows:

$$\cos\theta_{rough} = r \bullet \cos\theta_{smooth} \quad (1)$$

herein, r is the roughness factor meaning the ratio of rough surface area to planar/smooth surface area, where θ_{rough} is the contact angle of the rough surface and θ_{smooth} is the contact angle of the smooth surface [40,41]. Comparing the r values of each Ni-electrodeposited layer, Ni-electrodeposited (COOH-MWCNT/TREN)$_{20}$/Si wafer showed approximately 2.2- and 4.6-times larger surface area than Ni-electrodeposited MWCNT-free Au/Si wafer and bare Ni plate, respectively (Fig. S9). That is, when Ni was electrodeposited onto a less conductive MWCNT nanobundle-coated Si wafer with relatively a high sheet resistance, the Ni layer was assembled onto the substrate, forming a highly nanoprotuberant structure. On the other hand, the Ni electrodeposition onto a highly conductive substrate with a flat surface induced the formation of a smooth morphology on the surface with a relatively low surface area. As a result, these findings clearly indicate that MWCNT-induced Ni electrodeposition can significantly increase the

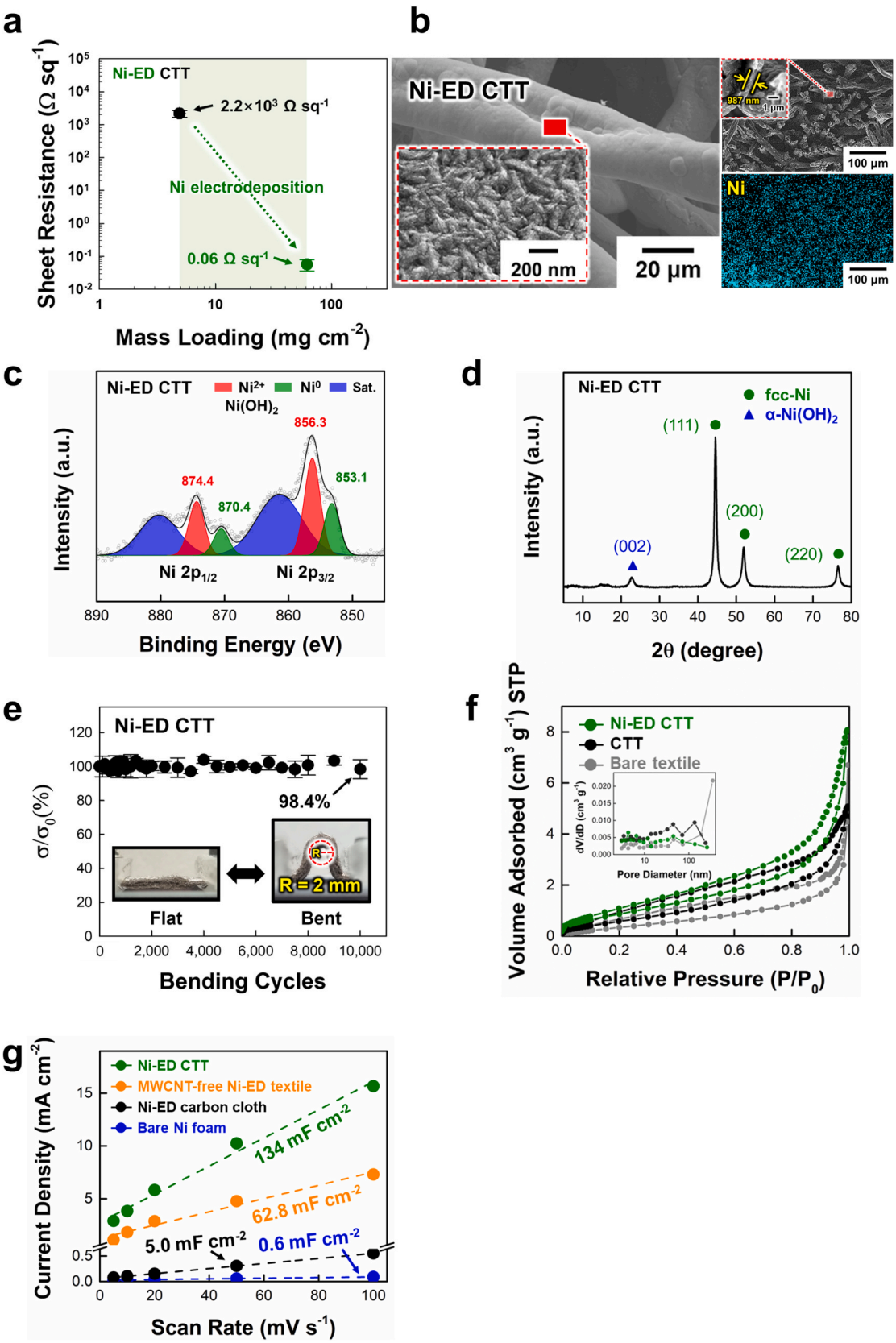

Fig. 2. Characterization of the Ni-ED CTT. a) Change in electrical properties of the Ni-ED CTT before and after the Ni electrodeposition. b) Planar/cross-sectional FE-SEM images at different degrees of magnification and corresponding EDS mapping image of Ni-ED CTT. c) Ni 2p high-resolution XPS spectra and d) XRD pattern of Ni-ED CTT. e) Mechanical stability test of Ni-ED CTT measuring relative electrical conductivity (σ/σ_0) as a function of a bending cycles with bending radius of about 2 mm. f) N_2 adsorption-desorption isotherms and corresponding pore size distribution (inset) of the bare textile, CTT, and Ni-ED CTT. g) Capacitive currents of Ni-ED CTT, MWCNT-free Ni-ED textile, Ni-ED carbon cloth, and bare Ni foam with increasing scan rate for calculation of double layer capacitances (C_{dl}).

surface area of textile electrodes. Furthermore, considering that Ni alloys such as NiMo (for HER) or NiFe (for OER), which have high electrocatalytic activities and stability [28,42], can be electrodeposited onto the entire surface from the exterior to the interior of Ni-ED CTT, it is reasonable to infer that the large surface area of Ni-ED CTT offers the possibility of notably enhancing its electrocatalytic performance.

3.3. NiMo-electrodeposited textile for HER electrode

It is widely recognized that NiMo alloy electrocatalysts exhibit excellent HER performance due to their ability to effectively decrease the energy barrier of the Volmer step and accelerate the slow HER kinetics in alkaline conditions [43–45]. Based on these electrocatalytic properties, NiMo was electrodeposited onto the Ni-ED CTT to prepare a high-performance HER textile electrode by optimizing electrodeposition time (**Fig. S10**). The resulting electrodeposited NiMo layer had a thickness of approximately 112 nm (*i.e.*, the total thickness of electrodeposited NiMo/Ni layer was ~1.10 μm), and the average mass loading amount of NiMo was 4.5 mg cm^{-2}, maintaining a highly porous 3D textile structure without blocking any pores (Fig. 3a). In addition, the electrodeposited NiMo layer exhibited highly nanoprotuberant surface morphology, which could effectively induce a large active surface area. The chemical composition of NiMo layer was estimated to be approximately 1: 0.12 Ni to Mo, with mainly existing in the form of Ni^0 (with some as Ni^{2+}) and Mo^{6+} (with some as Mo^{5+}, Mo^{4+}, Mo^0), respectively, as confirmed by XPS (Fig. 3b) [43,46]. The XRD pattern of NiMo showed the characteristic (111), (200), and (220) peaks of fcc NiMo, which exactly coincided with Ni crystal structure (Fig. S11) [46,47]. The structure was also observed in the HR-TEM and EDS mapping images, which showed the (111) plane and a 2.0 Å d-spacing of NiMo (**Fig. S12**). Additionally, the sheet resistance of NiMo-ED textile was measured to be approximately 0.08 Ω sq^{-1}—, which was comparable to that of the Ni-ED textile (0.06 Ω sq^{-1}). Furthermore, the NiMo-ED CTT CTT (*i.e.*, NiMo/Ni-ED CTT) maintained a considerably low skeletal mass density of 1.621 g cm^{-3} with a slight increase (~ 0.04 g cm^{-3}) compared to the Ni-ED CTT.

Based on these results, the HER performance of NiMo-ED was evaluated in 1 M KOH using a 3-electrode cell. In this case, the overpotentials of NiMo-ED CTT were measured to be approximately 8 and 203 mV at current densities of 10 and 1000 mA cm^{-2}, respectively, which outperformed those of MWCNT-free NiMo-ED textile (332 mV at 10 mA cm^{-2} and 251 mV at 1000 mA cm^{-2}), Ni-ED CTT (15 mV at 10 mA cm^{-2} and 305 mV at 1000 mA cm^{-2}), and conventional Pt/C-coated Ni foam electrode (19 mV at 10 mA cm^{-2} and 520 mV at 1000 mA cm^{-2}) under the same experimental conditions (Fig. 3**c, Supplementary detailed experimental procedures, and Table S1**). Additionally, a highly fluctuating polarization curve at high current density was observed in the MWCNT-free NiMo-ED textile with unfavorable interfacial interaction between the host electrode and NiMo electrocatalyst layer, which was in stark contrast to NiMo-ED CTT with a stable polarization curve at high current density. To the best of our knowledge, this extremely low overpotential (for HER) obtained from NiMo-ED CTT electrode has not been reported by other research groups.

Furthermore, the lower Tafel slope of NiMo-ED CTT (28.5 mV dec^{-1}) than those of other electrodes implied enhanced water-dissociation efficiency and identified rate-determining step (RDS) **(Fig. S13**). Generally, the HER mechanism in alkaline media is composed of a dissociation and recombination procedure [8,48]. During the water-splitting reaction, the dissociation process that occurs first is known as the Volmer step. In this step, water molecules (H_2O) are split into hydroxyl ions (OH^-) and hydrogen adsorbed onto a surface of the metal (*i.e.*, the absorbed hydrogen is an intermediate of water-splitting reaction, $2\ H_2O + M + 2e^- \leftrightarrows 2\ M\text{–}H_{ad} + 2OH^-$). Subsequently, the absorbed hydrogen undergoes a recombination process, but the recombination process can be either the Heyrovsky step ($H_2O + H_{ad}\text{-}M + e^- \leftrightarrows M + H_2 + OH^-$) or the Tafel step ($2\ M\text{–}H_{ad} \leftrightarrows 2\ M + H_2$). Herein, considering that the Tafel slope of NiMo-ED CTT in a low overpotential range (8 −30 mV) was 28.5 mV dec^{-1}, the NiMo-ED CTT electrode follows the Volmer-Tafel mechanism, and resultantly the Tafel step acts as an RDS for HER in the NiMo-ED CTT electrode.

We also confirmed the fast charge transfer kinetics of NiMo-ED CTT using EIS (Fig. 3d and Fig. S14). In this case, the charge transfer resistance (R_{ct}) of NiMo-ED CTT was measured to be 1.8 Ω, which was much lower than those of the other HER electrodes. To identify the electrochemically available surface area for HER between different electrodes, C_{dl} was estimated (Fig. S15) [45,49,50]. In this case, the C_{dl} values of NiMo-ED CTT (140 mF cm^{-2}—) and Ni-ED CTT (134 mF cm^{-2}) were almost similar, both being approximately 2.1 times larger than that of the MWCNT-free NiMo-ED textile (65.2 mF cm^{-2}), in line with above-mentioned difference in surface area between the electrodes with and without the MWCNT layer (see Fig. 2 g and Fig. S7). Additionally, the intrinsic catalytic activity of each electrode, excluding the effect of the surface area, was measured by normalizing the current density with ECSA. In this case, the intrinsic catalytic activities of NiMo-ED CTT and MWCNT-free NiMo-ED textile were similar to each other and showed approximately a 2.2-fold enhancement compared to that of Ni-ED CTT. These results suggest that the outstanding HER performance of NiMo-ED CTT was attributed to the extremely large active surface area (with aids of the nanoprotuberant structure of NiMo layer as well as microporous structure of fibrils) of the overall textile electrode and the high catalytic activity of NiMo alloy.

The NiMo alloy in our system also undergoes the reaction pathway with the optimized Gibbs free energy of H adsorption, which can have a significant effect on the HER performance. Generally, Ni is known as a metal element where hydrogen can be strongly adsorbed, but it is desirable for the adsorption strength of hydrogen on the Ni surface to be lowered for better electrocatalytic activity. In this view, Ni alloys such as NiMo can effectively decrease the hydrogen-Ni adsorption strength [44]. To explore this possibility, we first conducted an XPS analysis on the NiMo-ED CTT. The results showed that when Mo was alloyed with Ni, the Ni^0 peaks shifted to lower binding energies by 0.4 and 0.3 eV in Ni $2p_{1/2}$ and Ni $2p_{3/2}$ spectra, respectively (Fig. S16) [51]. This was mainly attributed to the reduction of Ni element, which was reported to weaken the hydrogen-binding energy as the *d*-band center of the metal shifted downward away from the Fermi level [52]. This phenomenon could also be demonstrated through X-ray absorption near-edge structure (XANES) analysis, as shown in Fig. 3e. In Ni K-edge XANES spectra, the white line intensity decreased from Ni-ED CTT to NiMo-ED CTT, indicating that the oxidation state of Ni in NiMo-ED CTT was reduced compared to that in Ni-ED CTT [53,54]. According to the electronegativity model of Allred-Rochow or Allen, the electronegativity of Ni has a higher value (1.75 on the Allred-Rochow scale and 1.88 on the Allen scale) than that of Mo (1.30 on the Allred-Rochow scale and 1.47 on the Allen scale) [55], which induces the transfer of electrons from Mo atom to Ni atom. As a result, the absorption pre-edge peak was negatively shifted (Fig. 3e and Fig. S17a). These findings were also consistent with the XPS analysis represented in Fig. S16.

To further investigate the local structure and atomic configuration, Fourier-transformed (FT) EXAFS was conducted **(Fig. S17b**). The predominant Ni-Ni first coordination shell main peak was slightly shifted to a larger reduced distance with the decreased intensity from Ni-ED CTT to NiMo-ED CTT. This shift indicated a reduction in Ni-Ni coordination and an increase in Ni-Ni bond length, which was attributed to the isolation effect of Mo atoms [45,56,57].

To better understand these phenomena, additional DFT calculations were carried out (**Supplementary detailed experimental procedures**). First, the energetically stable atomic structures of NiMo alloy were explored to model the catalytic activity of NiMo-ED CTT. Since the XRD pattern of NiMo-ED CTT was consistent with that of fcc Ni, this work excluded intermetallic compounds of NiMo alloys, such as Ni_3Mo and Ni_4Mo. Instead, all possible symmetrically inequivalent combinations (a total of 70 cases) of Mo substitution in the fcc Ni surface from the

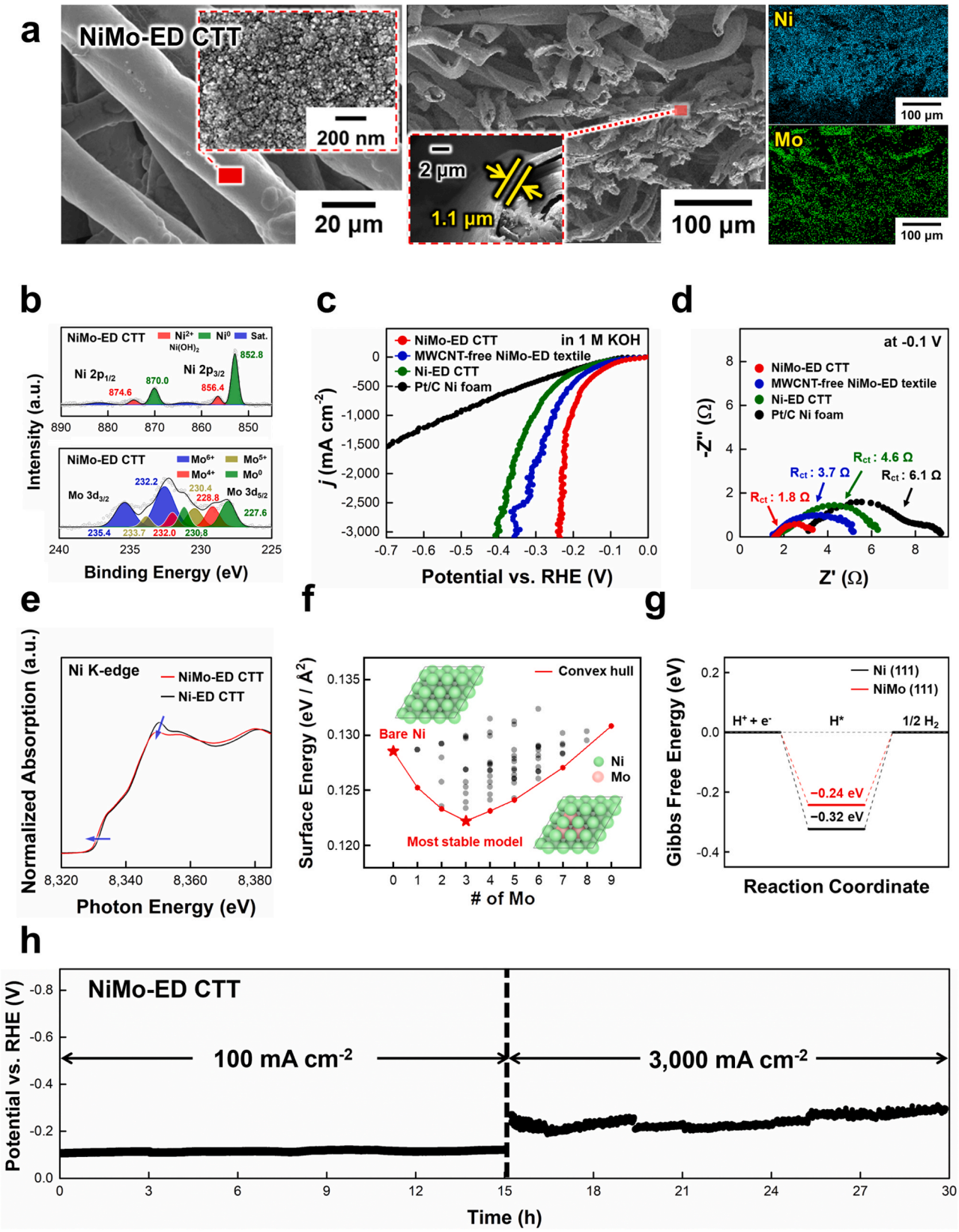

Fig. 3. Characterization and electrocatalytic performance of the NiMo-ED CTT. a) Planar/cross-sectional FE-SEM images at different degrees of magnification and corresponding EDS mapping images of the NiMo-ED CTT. b) Ni 2p and Mo 3d high-resolution XPS spectra of the NiMo-ED CTT. c) The HER polarization curves and d) EIS plots of NiMo-ED CTT, MWCNT-free NiMo-ED textile, Ni-ED CTT, and Pt/C Ni foam. EIS plots were measured at an applied potential of − 0.1 V (*vs.* RHE). e) Ni K-edge XANES spectra of thr NiMo-ED CTT, Ni-ED CTT. f) The surface free energy as a function of the number of substituted Mo atoms in Ni (111). g) Gibbs free energy diagram of HER on Ni (111) and NiMo (111). h) The chronopotentiometry stability test of NiMo-ED CTT at 100 mA cm^{-2} for 15 h and 3000 mA cm^{-2} for 15 h.

1st nearest neighbor to the 3rd nearest neighbor of the H adsorption site (*i.e.*, a fcc-hollow site), were considered as shown in Fig. S18. The surface free energies of all NiMo alloy model structures were then calculated and plotted as a function of the number of Mo substitutions in the fcc Ni surface (Fig. 3 f). In this case, the study revealed that the NiMo surface, which has 3 Mo substitutions in the 3rd nearest neighbor of the H adsorption site (hereafter referred to as NiMo (111)) has the lowest surface free energy. This result suggests that NiMo (111) is the most thermodynamically preferred surface among all the NiMo alloy models considered in this work. Subsequently, the DFT calculation of the Gibbs free energy of H adsorption was performed on NiMo (111) and bare Ni (111) to evaluate the overall performance of HER (Fig. 3 g). In this case, the Gibbs free energy calculations of H adsorption suggested that the excellent HER performance of NiMo-ED CTT could be attributed to the lower Gibbs free energy of H adsorption on NiMo(111) (−0.24 eV), which was closer to the optimal value for HER (0 eV), compared to that for Ni(111) (−0.32 eV).

Based on these results, the electrochemical stability of NiMo-ED CTT was further investigated through chronopotentiometry tests at current densities of 100 mA cm^{-2} for 15 h and 3000 mA cm^{-2} for 15 h. During the HER stability test, the potential of NiMo-ED CTT remained constant without any significant decay (Fig. 3 h**)**. Although additional oxidations were observed at the surface of the electrode after the harsh HER stability test (as revealed by the XPS spectra and FE-SEM image) (**Fig. S19 and S20),** they had no significant impact on the operational stability. Notably, it should be pointed out that an HER electrode, which can withstand such a high current density of 3000 mA cm^{-2}—, has not been reported until now. As a result, NiMo-ED CTT exhibited superior HER performance in terms of overpotential, Tafel slope, and durability, when compared to previously reported Ni nanocomposite electrodes with mixed metal components such as Ni_2N-NiMoN, Ni_2P/Ni, and $NiMoO_2$/Ni [11,12,18]. The outstanding performance was mainly attributed to the unique structural design and all-in-one interfacial engineering, as well as the intrinsically high catalytic activity of the electrodeposited NiMo layer.

3.4. NiFe-electrodeposited textile for OER electrode

Four electron-involved OER that generates O_2 and H_2O is a far more complex reaction process than two electron-involved HER that produces H_2 and OH^- ions. Therefore, the overall kinetics of the electrolytic water-splitting reaction is significantly limited by the sluggish OER at the anode, rather than HER at the cathode [58,59]. To address this problem and develop a high-performing OER electrode, we attempted to prepare an OER textile electrode using a NiFe layer, which is known as an active OER catalyst in alkaline media.

For achieving this goal, we fabricated NiFe/Ni-ED CTT (*i.e.*, NiFe-ED CTT) by electrodepositing the NiFe layer onto Ni-ED CTT, while adjusting electrodeposition time to optimize performance (Fig. S21). The surface morphology and structure of NiFe-ED CTT were investigated using FE-SEM and EDS mapping images (Fig. 4a). As with NiMo-ED textiles, the EDS images of FE-SEM exhibited uniform coating of Ni and Fe onto the Ni-ED CTT, preserving the original textile structure characterized by high porosity. Significantly, the electrodeposited NiFe layer exhibited a highly nanowrinkled structure with a thickness of approximately 283 nm (*i.e.*, the total thickness of electrodeposited NiFe/Ni layer was ~1.27 μm), and the average mass loading amount of NiFe was 4.3 mg cm^{-2}. This is a significant improvement compared to the typical NiFe layer prepared using hydrothermal method, which showed a wrinkled structure with a relatively large size [60].

Additionally, we investigated the chemical composition of NiFe-ED CTT with XPS. As shown in Fig. 4b, the Ni and Fe in the electrodeposited NiFe alloy mainly existed in the form of Ni^{2+} (at 856.4 and 874.6 eV for $Ni(OH)_2$) and Fe^{3+} (at 711.8 and 724.1 eV), respectively in the ratio of approximately 1:0.8 Ni to Fe [60,61,63,64]. Additionally, these peaks associated with the presence of Ni^{2+} and Fe^{3+} originated from major components of NiFe LDH.

To further confirm the chemical and surface structure of NiFe-ED CTT, we also performed the XRD and HR-TEM analysis. The (003), (006), and (012) peaks corresponding to the NiFe LDH were evidently distinguished from those (*i.e.*, (111), (200), and (220) peaks) of fcc Ni that originated from electrodeposited Ni layer of Ni-ED CTT (Fig. 4c) [61–63,65]. The HR-TEM images showed d-spacings of 2.5 and 3.8 Å, which are assigned to (012) and (006) planes, respectively (Fig. S22) [61,62]. This lattice structure matched well with the NiFe LDH peaks observed in the XRD pattern. Additionally, the NiFe-ED CTT maintained a remarkably low skeletal mass density of 1.619 g cm^{-3}, which was comparable to that of the NiMo-ED CTT.

Based on these results, we evaluated the OER performance of NiFe-ED CTT, MWCNT-free NiFe-ED textile, Ni-ED CTT, and conventional IrO_2-coated Ni foam in 1 M KOH condition using a 3-electrode cell (Table S2). During OER measurement, the generation of capacitive current and the appearance of peaks during oxidation can make it difficult to exactly monitor the catalytic activity of NiFe-ED CTT electrodes. To alleviate this issue, the effect of capacitive and oxidation current was reduced by averaging the forward and reverse sweeps of the CV curves (Fig. S23). In this case, the NiFe-ED CTT exhibited remarkably low overpotentials of 189, 202, and 227 mV at current densities of 50, 100, and 1000 mA cm^{-2}, respectively, outperforming the other electrodes (Fig. 4**d**). Specifically, the MWCNT-free NiFe-ED textile had overpotentials of approximately 227, 241, and 307 mV at 50, 100, and 1000 mA cm^{-2}, respectively, and additionally, the Ni-ED CTT exhibited the overpotential values of 285, 301, and 384 mV at 50, 100, and 1000 mA cm^{-2}, respectively. The overpotential values of IrO_2-coated Ni foam were measured to be 316, 334, and 497 mV at 50, 100, and 1000 mA cm^{-2}, respectively. Additionally, we investigated OER catalytic performance using a graphite rod-based counter electrode instead of Pt counter electrode. In this case, the overpotential values of OER electrodes measured using a graphite rod were slightly higher than those of OER electrode measured using a Pt-based counter electrode, which were mainly attributed to the better performances (*i.e.*, electrocatalytic property, electrical conductivity, and surface area) of Pt mesh as counter electrode (**Fig. S24**).

Additionally, the OER kinetics of NiFe-ED CTT electrode was superior to those of MWCNT-free NiFe-ED textile, Ni-ED CTT, and IrO_2 Ni foam, as confirmed by its Tafel slope (30.1 mV dec^{-1}) and electrochemical resistances measured using EIS measurement (Fig. 4e, Fig. S25, Fig. S26, and Supplementary detailed experimental procedures). Particularly, in the case of electrochemical resistances, the NiFe-ED CTT exhibited R_{ct} and R_s of approximately 0.9 Ω and 1.8 Ω, respectively, significantly lower than those of other electrodes. Here, the metal electrodeposited CTT shown in our study was free from the effects of carbon corrosion that is detrimental to the electrochemical performance. This is because the MWCNT sublayers adsorbed on the surface of the cotton textile were completely encapsulated by electrodeposited Ni/NiFe layers with a thickness of approximately 1.27 μm (Fig. S27).

To gain further insight into the improved OER performance of NiFe-ED CTT electrodes, we estimated the ECSA of the electrodes using C_{dl}. To calculate C_{dl}, we measured CV curves at 0.95 − 1.05 V (Fig. S28) [66,67]. Interestingly, the C_{dl} of NiFe-ED CTT was estimated to be 112 mF cm^{-2}, which was 1.2 times larger than that of the Ni-ED CTT (92.4 mF cm^{-2}) and 2.3 times larger than that of the MWCNT-free NiFe-ED textile (48.8 mF cm^{-2}). Consistent with the C_{dl} results of NiMo-ED CTT and MWCNT-free NiMo-ED textile electrodes (see Fig. S15), the incorporated MWCNT layer caused an approximately two-fold increase in active surface area. Additionally, the observed increase in surface area after NiFe electrodeposition was primarily due to the nanowrinkled structure of NiFe LDH as well as the extremely porous fibrillar structure of the textile electrode. This increase in active surface area, combined with the excellent catalytic activity of NiFe, strongly contributed to the high OER performance of NiFe-ED CTT.

Furthermore, we attempted to establish and elucidate the active sites

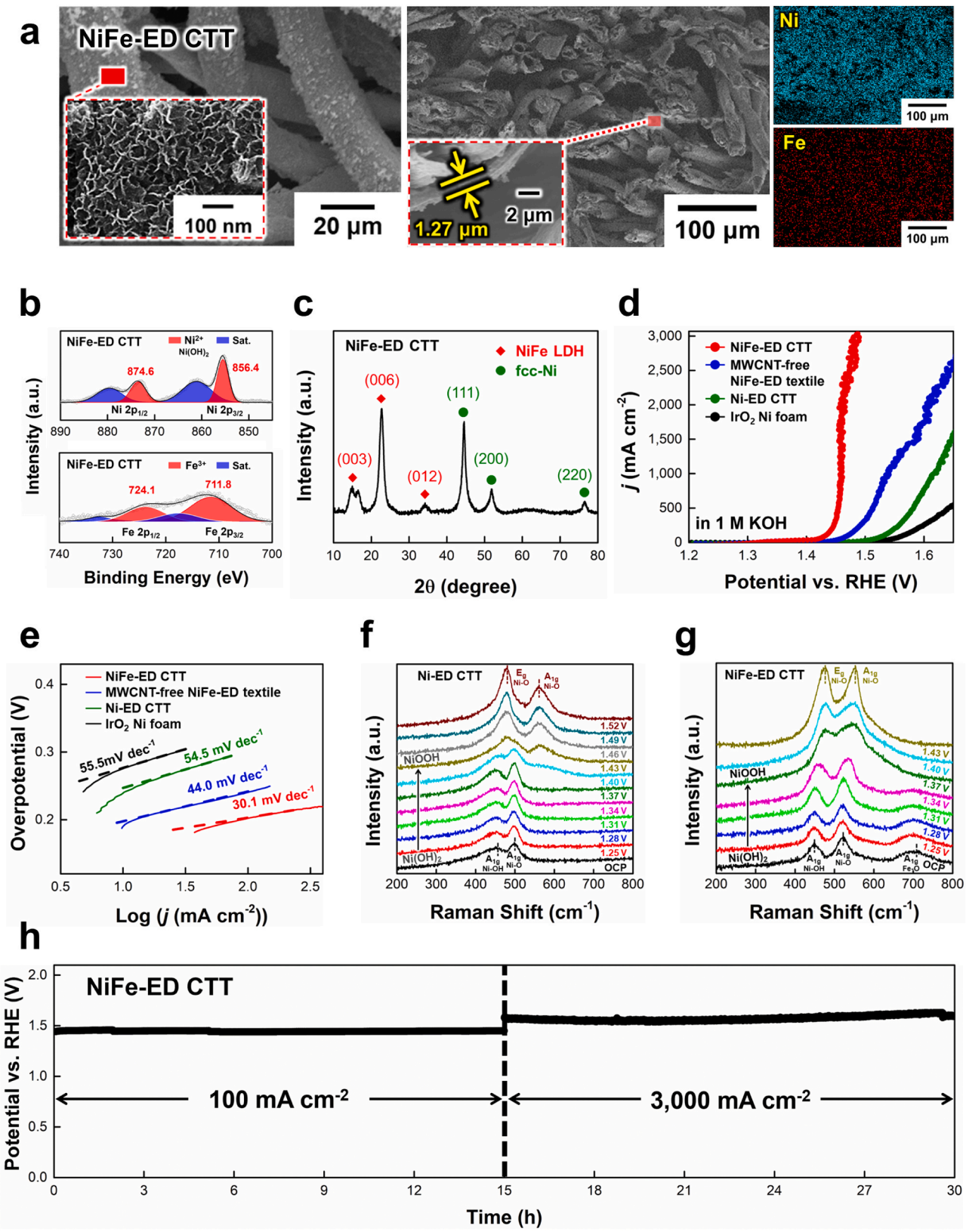

Fig. 4. Characterization and electrocatalytic performance of the NiFe-ED CTT. a) Planar/cross-sectional FE-SEM images at different degrees of magnification and corresponding EDS mapping images of the NiFe-ED CTT. b) Ni 2p and Fe 2p high-resolution XPS spectra and c) XRD pattern of the NiFe-ED CTT. d) The OER polarization curves and e) Tafel plots of the NiFe-ED CTT, MWCNT-free NiFe-ED textile, Ni-ED CTT, and IrO_2 Ni foam. *Operando* Raman spectra of the f) Ni-ED CTT and g) NiFe-ED CTT under OER conditions. h) The chronopotentiometry stability test of NiFe-ED CTT at 100 mA cm^{-2} for 15 h and 3000 mA cm^{-2} for 15 h.

of NiFe-ED CTT for OER using *operando* Raman analysis. Fig. 4f,g showed the Raman spectral changes of Ni-ED CTT and NiFe-ED CTT recorded at various applied potentials. At open circuit potential, Ni-ED CTT exhibited two peaks at 450 cm^{-1} and 495 cm^{-1}, corresponding to the $A_{1\,g}$ stretching modes of Ni-OH and Ni-O in $Ni(OH)_2$, respectively (see Fig. 4f). As the applied potential increased up to 1.52 V *vs.* RHE, the $A_{1\,g}$ stretching mode peaks became stronger and eventually disappeared due to the formation of NiOOH, which detected by the E_g bending and $A_{1\,g}$ stretching modes of Ni-O in NiOOH at 479 cm^{-1} and 560 cm^{-1}, respectively [60,65]. On the other hand, the *operando* Raman spectra of NiFe-ED CTT revealed different local structure changes during the OER process. As shown in Fig. 4g, the three obvious peaks could be assigned to the vibration of Ni-OH at 449 cm^{-1} and Ni-O in disordered $Ni(OH)_2$ at 520 cm^{-1}, respectively [70], with the vibration of Fe-O at 700 cm^{-1} in FeOOH, which appeared by the interaction between OH^- and Fe^{3+} at low potentials [68,71–73]. Importantly, the Ni-OH and Ni-O vibration in NiFe-ED CTT was gradually transformed to the E_g bending (474 cm^{-1}) and $A_{1\,g}$ stretching (552 cm^{-1}) modes of Ni-O in NiOOH at lower potential (1.43 V *vs.* RHE) compared to Ni-ED CTT (1.52 V *vs.* RHE), representing the facile formation of NiOOH during the OER process. Moreover, the peak positions and intensity ratios of the E_g bending and $A_{1\,g}$ stretching modes of Ni-O in the formed NiOOH intermediate for Ni-ED CTT and NiFe-ED CTT provide valuable information about the local structure of Ni-O and the interlayer distance. That is, the formed NiOOH in NiFe-ED CTT (474 cm^{-1} and 552 cm^{-1}) was detected at lower wavenumbers than those of Ni-ED CTT (479 cm^{-1} and 560 cm^{-1}) due to the elongated Ni-O bond, which might be related to the disordered structure. In addition, the E_g bending/$A_{1\,g}$ stretching intensity ratio of NiFe-ED CTT ($I_{474}/I_{552} = 1.03$) was significantly lower than that of Ni-ED CTT ($I_{479}/I_{560} = 1.66$), which strongly correlated to the formation of the β-NiOOH phase in the anodic process [69,74]. Therefore, the outstanding OER catalytic activity of NiFe-ED CTT could be attributed to the rapid formation of NiOOH intermediates with the desirable β-NiOOH phase that was highly active for OER as well as the structural effect of the textile electrode with a large active surface area.

To support the experimental finding that the OER kinetics of NiFe-ED CTT outperform those of Ni-ED CTT, we performed additional DFT calculations to determine the Gibbs free energy along the OER pathway for both Ni LDH and NiFe LDH structures (**Fig. S29a and Supplementary detailed experimental procedures**). For Ni LDH, the theoretical overpotential was calculated to be 1.48 V. In this case, the *OH →*O step serves as the RDS due to weak adsorption of OH and even weaker adsorption of O. Conversely, when Fe is incorporated into Ni LDH, the overpotential is significantly reduced to 0.53 V (**Fig. S29b**). This improvement is attributed to the strengthened adsorption of both OH and O in leading to a change in the RDS to *O → *OOH, facilitated by the presence of Fe, which acts as an active site for OER. These findings are in line with previously reported literature [75,76]. Therefore, the incorporation of Fe, serving as additional active sites for the OER, could be one of the key factors contributing to the superior OER performance of our NiFe-ED CTT.

Based on these results, we investigated the electrochemical stability of NiFe-ED CTT through harsh chronopotentiometry tests (at 100 mA cm^{-2} for 15 h and 3000 mA cm^{-2} for 15 h) as shown in Fig. 4h. Despite observing slight oxidation from Ni^{2+} to Ni^{3+} in the XPS spectra of NiFe-ED CTT after the operational stability test, the surface morphology and overall potential of the electrode remained stable and maintained its initial potential value without any significant change (Fig. S30 and S31). These results also indicate that the robust electrocatalytic layers of NiFe-ED CTT as an OER electrode, as well as NiMo-ED CTT as an HER electrode, are highly stable due to the formation of an all-in-one fibril-type structure induced by favorable interfacial interactions.

3.5. Full-cell water electrolyzer composed of HER and OER textile electrodes

Based on the remarkable performances of the HER and OER textile electrodes, we prepared a full-cell water-splitting device composed of NiMo-ED CTT cathode (for HER) and NiFe-ED CTT anode (for OER) (Movie S1). Initially, our focus was to validate that the microstructural flaws in the acid-treated CTT and COOH-MWCNT had an insignificant impact on the electrocatalytic properties of NiMo-ED CTT and NiFe-ED CTT. This led us to investigate the structural characteristics of pristine MWCNT, CTT, COOH-MWCNTs, NiMo-ED CTT, and NiFe-CTT using Raman spectroscopy (Fig. S32). The Raman spectra of these distinct samples exhibited prominent peaks at approximately 1340 and 1590 cm^{-1}, corresponding to the D band (arising from the disordered $A_{1\,g}$ vibrational mode of hexagonal carbon structures) and the G band (stemming from the $E_{2\,g}$ vibrational mode of six-membered aromatic rings), respectively. Remarkably, the D/G band ratios were similar across all samples except pristine MWCNT, implying that the electrocatalytic process of the complete-cell devices remained unaffected by the structural defects present in CTT and COOH-MWCNTs embedded within both HER and OER electrodes.

Similar to the OER measurement, the polarization curves of the full-cell water-splitting devices were obtained by averaging the measured values of the forward and reverse sweeps of the CV curves, effectively reducing the influence of capacitive current and Ni oxidation current (**Fig. S33**). In this case, the NiMo-ED CTT cathode‖NiFe-ED CTT anode (shortly, NiMo-ED CTT‖NiFe-ED CTT) delivered current densities of 10, 100, 1000 and 3000 mA cm^{-2} at relatively low cell voltages of 1.34, 1.55, 1.77, and 2.01 V, respectively, which were much higher than those of the MWCNT-free NiMo-ED textile‖MWCNT-free NiFe-ED textile-based device, Ni-ED CTT‖Ni-ED CTT-based device, and the Pt/C Ni foam‖IrO_2 Ni foam-based device at the same cell voltages (Fig. 5a and Table S3). Furthermore, this remarkable high performance of the NiMo-ED CTT‖NiFe-ED CTT device outperformed that of previously reported full-cell devices based on nonnoble metal catalysts in alkaline media (Fig. 5b) [9–15].

Additionally, we confirmed the unprecedentedly high operational stability of NiMo-ED CTT‖NiFe-ED CTT through a chronopotentiometry test. Specifically, when the current density was varied from 10 to 3000 mA cm^{-2}, the cell voltage of the device remained constant for defined time intervals and could be maintained for at least 2000 h (Fig. 5c and Fig. S34). However, unlike the CTT-based cell, the MWCNT-free NiMo-ED textile‖MWCNT-free NiFe-ED textile cell showed increasing and fluctuating potential during operation at 3000 mA cm^{-2} (Fig. 5d). Notably, this long-term durability of the CTT-based cell at an exceptionally high current density of 3000 mA cm^{-2} has not been reported to date by other research groups. After the stability test, we also investigated the states of each electrode and electrolyte. First, the compositions of both NiMo-ED CTT and NiFe-ED CTT were almost similar to those of the electrodes before the stabilty test. Additionally, when comparing the XPS spectra of the electrodes after 2000 h in the full-cell stability test with those of the electrodes after 30 h in the half-cell stability test, they showed nearly identical oxidation tendencies (Fig. S35).

Based on these XRD results, we confirmed that NiMo-ED CTT could maintain highly stable electrocatalystic structure even after the harsh stabilty test, and on the other hand, the crystalinity of the NiFe-ED CTT was slightly decreased (**Fig. S36**). In terms of the electrolyte, Ni, Mo, and Fe ions were not detected after 20 h operation at a high current density of 3000 mA cm^{-2}, as confirmed by ICP-MS (Table S4). Furthermore, we investigated the faradaic efficiency of NiMo-ED CTT‖NiFe-ED CTT device through the comparison of experimentally measured products (*i.e.*, generated H_2 and O_2 gases) and theoretically calculated products (*i.e.*, calculated H_2 and O_2 amounts from charges passed at given time intervals). In this case, the faradaic efficiency of HER and OER electrodes was estimated to be approximately 99.7% and 98.9%, respectively

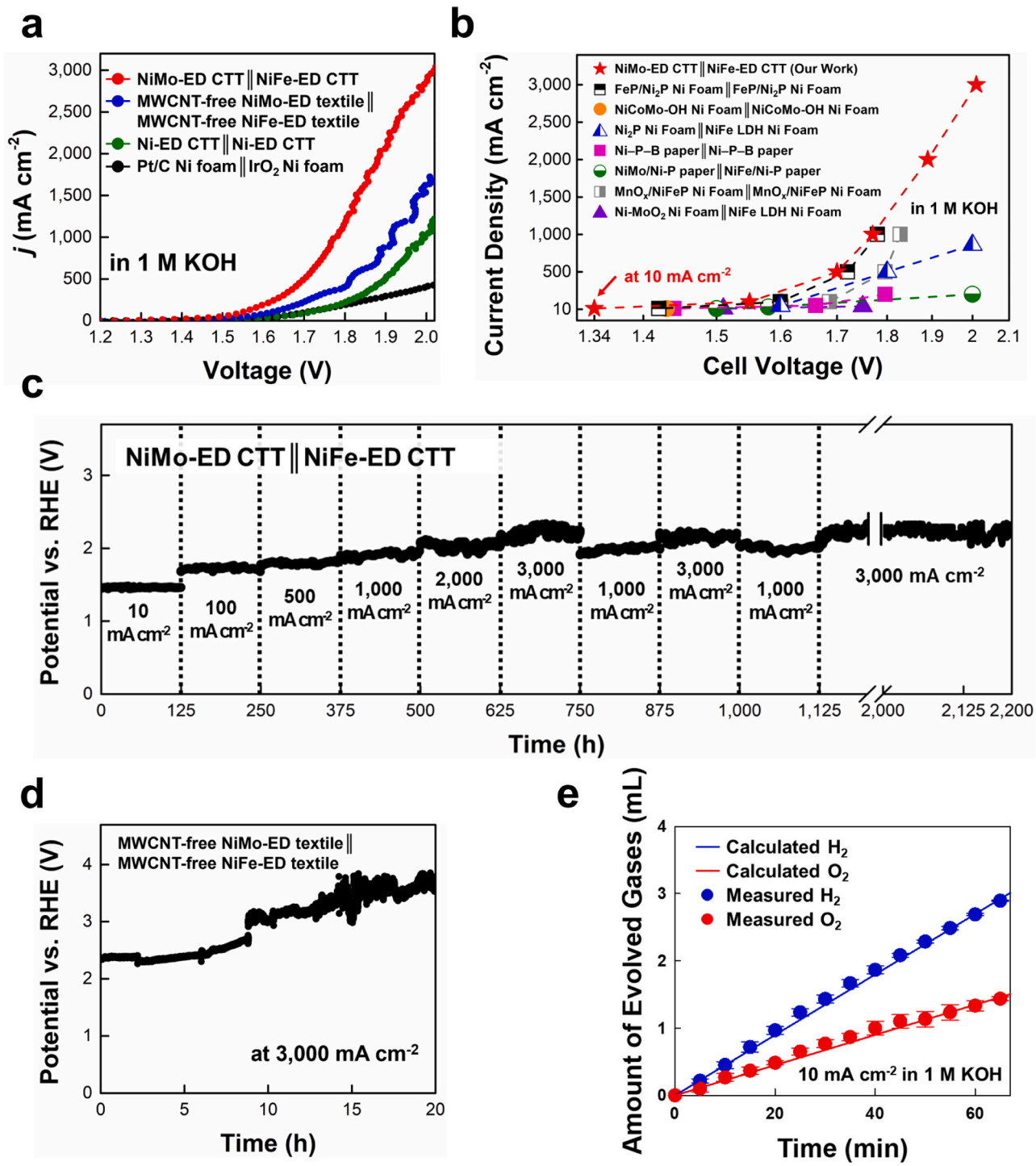

Fig. 5. Overall performance of the full-cell water-splitting electrodes. a) Polarization curves of the NiMo-ED CTT‖NiFe-ED CTT electrodes, MWCNT-free NiMo-ED textile‖MWCNT-free NiFe-ED textile electrodes, Ni-ED CTT‖Ni-ED CTT electrodes, and Pt/C Ni foam‖IrO_2 Ni foam electrodes. b) Comparison of cell voltages between the NiMo-ED CTT‖NiFe-ED CTT electrodes (in our work) and other nonnoble metal-based water-splitting electrodes (reported by other research groups). c) Chronopotentiometry stability test of the NiMo-ED CTT‖NiFe-ED CTT electrodes recorded at 10 mA cm^{-2}, 100 mA cm^{-2}, 500 mA cm^{-2}, 1000 mA cm^{-2}, 2000 mA cm^{-2}, and 3000 mA cm^{-2}. d) Chronopotentiometry curve of MWCNT-free NiMo-ED textile‖MWCNT-free NiFe-ED textile cell at current density of 3000 mA cm^{-2}. e) Theoretically calculated and experimentally measured amounts of H_2 and O_2 gases from NiMo-ED CTT‖NiFe-ED CTT as a function of the interval time at a constant current density of 10 mA cm^{-2}.

(Fig. 5e, Fig. S37, and Supplementary detailed experimental procedures). We also confirmed that these full-cell electrodes could maintain high water-splitting performance in a harsher electrolyte environment (30 wt% KOH solution at 60 °C) corresponding to commercially available conditions (Fig. S38). Additionally, it is worth noting that our approach is highly advantageous for large-scale water-splitting textile electrodes (Fig. S39), which can be applied to various substrates various substrates including polyester, nylon, silk, and paper as well as cotton (Fig. S40).

4. Conclusions

In conclusion, we have successfully converted insulating textiles into high-performance electrocatalytic textiles through a small molecule-driven assembly of MWCNTs and subsequent electrodeposition of non-noble metals. The resulting textile electrodes exhibit a perfect fibrillar structure and nanostructured surface morphology, featuring nano-protuberant and nanowrinkled structures. These electrodes demonstrate exceptional performance for the HER and the OER, achieving remarkably low overpotentials of 8 mV at 10 mA cm^{-2} for HER and 189 mV at 50 mA cm^{-2} for OER. Moreover, they exhibit long-term operational stability, maintaining their performance for at least 2000 h under high current densities ranging from 10 to 3000 mA cm^{-2}. As a result, our findings indicate that the outstanding water-splitting performances can be attributed to the all-in-one structured NiMo and NiFe electrodes, which possess a large active surface area and intrinsically high catalytic activity. This conclusion is supported by *in-situ/operando* electrocatalyst characterization and DFT calculations. Notably, our designed textile electrodes facilitate highly favorable interfacial interactions at all interfaces, including between the pristine textile and conductive seed (MWCNT/TREN multilayer), between the conductive seed and electrodeposited metal layer, and between the electrodeposited metal layer and electrocatalysts. This approach provides a valuable tool for the development and design of various high-performance electrochemical 3D electrodes, including water-splitting electrodes, that require a large specific surface area and robust interfacial interactions.

CRediT authorship contribution statement

Kwon Cheong Hoon: Investigation, Methodology. **Ju Hyun:** Investigation, Methodology. **Kim Gyuchan:** Data curation, Methodology. **Lee Wonyoung:** Data curation, Investigation, Methodology. **Ahn Jeongyeon:** Investigation, Methodology. **Mo Jeongmin:** Data curation, Investigation, Methodology. **Yong Euiju:** Formal analysis, Methodology. **Kim Myeongjin:** Formal analysis, Investigation, Methodology, Supervision, Writing – original draft, Writing – review & editing. **Cho Jinhan:** Conceptualization, Formal analysis, Funding acquisition, Investigation, Methodology, Project administration, Supervision, Validation, Visualization, Writing – original draft, Writing – review & editing. **Son Youhyun:** Conceptualization, Data curation, Formal analysis, Investigation, Methodology, Validation, Visualization, Writing – original draft, Writing – review & editing. **Lee Seung Woo:** Data curation, Methodology. **Kim Byung-Hyun:** Investigation, Methodology, Supervision, Writing – original draft.

Declaration of Competing Interest

The authors declare that they have no known competing financial interests or personal relationships that could have appeared to influence the work reported in this paper.

Data Availability

Data will be made available on request.

Acknowledgements

This work was supported by a National Research Foundation of Korea (NRF) grant funded by the Korea government (Ministry of Science and ICT) (NRF-2021R1A2C3004151, 2021R1A4A1031761, and 2022R1A2C1009690). We also acknowledge support from KIST Institutional Program (2V09840-23-P025) and the KU-KIST Graduate School of Converging Science and Technology Program.

Appendix A. Supporting information

Supplementary data associated with this article can be found in the online version at doi:10.1016/j.apcatb.2023.123563.

References

[1] J.A. Turner, A Realizable renewable energy future, Science 285 (1999) 687, https://doi.org/10.1126/science.285.5428.687.
[2] J.A. Turner, Sustainable hydrogen production, Science 305 (2004) 972, https://doi.org/10.1126/science.110319.
[3] S. Chu, A. Majumdar, Opportunities and challenges for a sustainable energy future, Nature 488 (2012) 294–303, https://doi.org/10.1038/nature11475.
[4] S.Y. Tee, K.Y. Win, W.S. Teo, L.-D. Koh, S. Liu, C.P. Teng, M.-Y. Han, Recent progress in energy-driven water splitting, Adv. Sci. 4 (2017), 1600337, https://doi.org/10.1002/advs.201600337.
[5] Q. Xu, J. Zhang, H. Zhang, L. Zhang, L. Chen, Y. Hu, H. Jiang, C. Li, Atomic heterointerface engineering overcomes the activity limitation of electrocatalysts and promises highly-efficient alkaline water splitting, Energy Environ. Sci. 14 (2021) 5228–5259, https://doi.org/10.1039/D1EE02105B.
[6] Z.-Y. Yu, Y. Duan, X.-Y. Feng, X. Yu, M.-R. Gao, S.-H. Yu, Clean and affordable hydrogen fuel from alkaline water splitting: past, recent progress, and future prospects, Adv. Mater. 33 (2021), 2007100, https://doi.org/10.1002/adma.202007100.
[7] J.K. Nørskov, T. Bligaard, A. Logadottir, J.R. Kitchin, J.G. Chen, S. Pandelov, U. Stimming, Trends in the exchange current for hydrogen evolution, J. Electrochem. Soc. 152 (2005) J23, https://doi.org/10.1149/1.1856988.
[8] R. Subbaraman, D. Tripkovic, D. Strmcnik, K.-C. Chang, M. Uchimura, A. P. Paulikas, V. Stamenkovic, N.M. Markovic, Enhancing hydrogen evolution activity in water splitting by tailoring Li^{+}-$Ni(OH)_2$-Pt interfaces, Science 334 (2011) 1256, https://doi.org/10.1126/science.1211934.
[9] S. Hao, L. Chen, C. Yu, B. Yang, Z. Li, Y. Hou, L. Lei, X. Zhang, NiCoMo hydroxide nanosheet arrays synthesized via chloride corrosion for overall water splitting, ACS Energy Lett. 4 (2019) 952–959, https://doi.org/10.1021/acsenergylett.9b00333.
[10] P. Wang, Y. Luo, G. Zhang, M. Wu, Z. Chen, S. Sun, Z. Shi, MnO_x-decorated nickel-iron phosphides nanosheets: interface modifications for robust overall water splitting at ultra-high current densities, Small 18 (2022), 2105803, https://doi.org/10.1002/smll.202105803.
[11] G. Xiong, Y. Chen, Z. Zhou, F. Liu, X. Liu, L. Yang, Q. Liu, Y. Sang, H. Liu, X. Zhang, J. Jia, W. Zhou, Rapid synthesis of various electrocatalysts on Ni foam using a universal and facile induction heating method for efficient water splitting, Adv. Funct. Mater. 31 (2021), 2009580, https://doi.org/10.1002/adfm.202009580.
[12] X. Yu, Z.-Y. Yu, X.-L. Zhang, Y.-R. Zheng, Y. Duan, Q. Gao, R. Wu, B. Sun, M.-R. Gao, G. Wang, S.-H. Yu, Superaerophobic" nickel phosphide nanoarray catalyst for efficient hydrogen evolution at ultrahigh current densities, J. Am. Chem. Soc. 141 (2019) 7537–7543, https://doi.org/10.1021/jacs.9b02527.
[13] F. Yu, H. Zhou, Y. Huang, J. Sun, F. Qin, J. Bao, W.A. Goddard, S. Chen, Z. Ren, High-performance bifunctional porous non-noble metal phosphide catalyst for overall water splitting, Nat. Commun. 9 (2018), 2551, https://doi.org/10.1038/s41467-018-04746-z.
[14] A. Sahasrabudhe, H. Dixit, R. Majee, S. Bhattacharyya, Value added transformation of ubiquitous substrates into highly efficient and flexible electrodes for water splitting, Nat. Commun. 9 (2018), 2014, https://doi.org/10.1038/s41467-018-04358-7.
[15] W. Hao, R. Wu, H. Huang, X. Ou, L. Wang, D. Sun, X. Ma, Y. Guo, Fabrication of practical catalytic electrodes using insulating and eco-friendly substrates for overall water splitting, Energy Environ. Sci. 13 (2020) 102–110, https://doi.org/10.1039/C9EE00839J.
[16] J.-S. Li, S. Zhang, J.-Q. Sha, H. Wang, M.-Z. Liu, L.-X. Kong, G.-D. Liu, Confined molybdenum phosphide in p-doped porous carbon as efficient electrocatalysts for hydrogen evolution, ACS Appl. Mater. Interfaces 10 (2018) 17140–17146, https://doi.org/10.1021/acsami.8b01541.
[17] H. Yan, Y. Xie, A. Wu, Z. Cai, L. Wang, C. Tian, X. Zhang, H. Fu, Anion-modulated HER and OER activities of 3D Ni–V-based interstitial compound heterojunctions for high-efficiency and stable overall water splitting, Adv. Mater. 31 (2019), 1901174, https://doi.org/10.1002/adma.201901174.
[18] A. Wu, Y. Xie, H. Ma, C. Tian, Y. Gu, H. Yan, X. Zhang, G. Yang, H. Fu, Integrating the active OER and HER components as the heterostructures for the efficient overall water splitting, Nano Energy 44 (2018) 353, https://doi.org/10.1016/j.nanoen.2017.11.045.
[19] P. Chen, T. Zhou, M. Zhang, Y. Tong, C. Zhong, N. Zhang, L. Zhang, C. Wu, Y. Xie, 3D nitrogen-anion-decorated nickel sulfides for highly efficient overall water splitting, Adv. Mater. 29 (2017), 1701584, https://doi.org/10.1002/adma.201701584.
[20] X. Luo, P. Ji, P. Wang, R. Cheng, D. Chen, C. Lin, J. Zhang, J. He, Z. Shi, N. Li, S. Xiao, S. Mu, Interface engineering of hierarchical branched Mo-doped Ni_3S_2/Ni_xP_y hollow heterostructure nanorods for efficient overall water splitting, Adv. Energy Mater. 10 (2020), 1903891, https://doi.org/10.1002/aenm.201903891.
[21] J.-S. Li, J.-Y. Li, M.-J. Huang, L.-X. Kong, Z. Wu, Anchoring Ru_xP on 3D hollow graphene nanospheres as efficient and pH-universal electrocatalysts for the hydrogen evolution reaction, Carbon 161 (2020) 44–50, https://doi.org/10.1016/j.carbon.2020.01.049.
[22] S. Yang, J.-Y. Zhu, X.-N. Chen, M.-J. Huang, S.-H. Cai, J.-Y. Han, J.-S. Li, Self-supported bimetallic phosphides with artificial heterointerfaces for enhanced

electrochemical water splitting, Appl. Catal. B Environ. 304 (2022), 120914, https://doi.org/10.1016/j.apcatb.2021.120914.
[23] S.-H. Cai, X.-N. Chen, M.-J. Huang, J.-Y. Han, Y.-W. Zhou, J.-S. Li, Interfacial engineering of nickel/iron/ruthenium phosphides for efficient overall water splitting powered by solar energy, J. Mater. Chem. A 10 (2022) 772, https://doi.org/10.1039/D1TA08385F.
[24] F.M. Sapountzi, J.M. Gracia, C.J.K.-J. Weststrate, H.O.A. Fredriksson, J.W. H. Niemantsverdriet, Electrocatalysts for the generation of hydrogen, oxygen and synthesis gas, Prog. Energy Combust. Sci. 58 (2017) 1–35, https://doi.org/10.1016/j.pecs.2016.09.001.
[25] Y. Luo, Z. Zhang, M. Chhowalla, B. Liu, Recent advances in design of electrocatalysts for high-current-density water splitting, Adv. Mater. 34 (2022), 2108133, https://doi.org/10.1002/adma.202108133.
[26] J. Mo, Y. Ko, Y.S. Yun, J. Huh, J. Cho, A carbonization/interfacial assembly-driven electroplating approach for water-splitting textile electrodes with remarkably low overpotentials and high operational stability, Energy Environ. Sci. 15 (2022) 3815–3829, https://doi.org/10.1039/D2EE01510B.
[27] O.P. Watts, Rapid nickel plating, Trans. Am. Electrochem. Soc. 29 (1916) 395–403.
[28] C.C.L. McCrory, S. Jung, I.M. Ferrer, S.M. Chatman, J.C. Peters, T.F. Jaramillo, Benchmarking hydrogen evolving reaction and oxygen evolving reaction electrocatalysts for solar water splitting devices, J. Am. Chem. Soc. 137 (2015) 4347–4357.
[29] X. Lu, C. Zhao, Electrodeposition of hierarchically structured three-dimensional nickel–iron electrodes for efficient oxygen evolution at high current densities, Nat. Commun. 6 (2015) 6616.
[30] K. Esumi, M. Ishigami, A. Nakajima, K. Sawada, H. Honda, Chemical treatment of carbon nanotubes, Carbon 34 (1996) 279–281, https://doi.org/10.1016/0008-6223(96)83349-5.
[31] S.W. Lee, B.-S. Kim, S. Chen, Y. Shao-Horn, P.T. Hammond, Layer-by-layer assembly of all carbon nanotube ultrathin films for electrochemical applications, J. Am. Chem. Soc. 131 (2009) 671–679, https://doi.org/10.1021/ja807059k.
[32] J. Zhang, H. Zou, Q. Qing, Y. Yang, Q. Li, Z. Liu, X. Guo, Z. Du, Effect of chemical oxidation on the structure of single-walled carbon nanotubes, J. Phys. Chem. B 107 (2003) 3712–3718, https://doi.org/10.1021/jp027500u.
[33] S. Zanganeh, F. Khodadadei, S.R. Tafti, M. Abdolahad, Folic acid functionalized vertically aligned carbon nanotube (FA-VACNT) electrodes for cancer sensing applications, J. Mater. Sci. Technol. 32 (2016) 617–625, https://doi.org/10.1016/j.jmst.2016.05.001.
[34] S. Lee, Y. Song, Y. Ko, Y. Ko, C.H. Kwon, J. Huh, S.-W. Kim, B. Yeom, J. Cho, A metal-like conductive elastomer with a hierarchical wrinkled structure, Adv. Mater. 32 (2020), 1906460, https://doi.org/10.1002/adma.201906460.
[35] C. Ji, J. Bi, S. Wang, X. Zhang, S. Yang, Ni nanoparticle doped porous VN nanoflakes assembled into hierarchical hollow microspheres with a structural inheritance from the $Ni_{1-x}V_xO_2$ cathode material for high performance asymmetric supercapacitors, J. Mater. Chem. A 4 (2016) 2158–2168, https://doi.org/10.1039/C5TA10406H.
[36] N.J.S. Costa, R.F. Jardim, S.H. Masunaga, D. Zanchet, R. Landers, L.M. Rossi, Direct access to oxidation-resistant nickel catalysts through an organometallic precursor, ACS Catal. 2 (2012) 925–929, https://doi.org/10.1021/cs200609e.
[37] J. van Drunen, B. Kinkead, M.C.P. Wang, E. Sourty, B.D. Gates, G. Jerkiewicz, Comprehensive structural, surface-chemical and electrochemical characterization of nickel-based metallic foams, ACS Appl. Mater. Interfaces 5 (2013) 6712–6722, https://doi.org/10.1021/am401606n.
[38] N. Weidler, J. Schuch, F. Knaus, P. Stenner, S. Hoch, A. Maljusch, R. Schäfer, B. Kaiser, W. Jaegermann, X-ray photoelectron spectroscopic investigation of plasma-enhanced chemical vapor deposited NiO_x, $NiO_x(OH)_y$, and $CoNiO_x(OH)_y$: influence of the chemical composition on the catalytic activity for the oxygen evolution reaction, J. Phys. Chem. C. 121 (2017) 6455–6463, https://doi.org/10.1021/acs.jpcc.6b12652.
[39] J. Zhang, Y. Bai, C. Zhang, H. Gao, J. Niu, Y. Shi, Y. Zhang, M. Song, Z. Zhang, Hybrid $Ni(OH)_2$/FeOOH@NiFe nanosheet catalysts toward highly efficient oxygen evolution reaction with ultralong stability over 1000hours, ACS Sustain. Chem. Eng. 7 (2019) 14601–14610, https://doi.org/10.1021/acssuschemeng.9b02296.
[40] R.N. Wenzel, Resistance of solid surfaces to wetting by water, Ind. Eng. Chem. 28 (1936) 988–994, https://doi.org/10.1021/ie50320a024.
[41] F. Yang, Heterogeneous nucleation of an embryo in the shape of square prism: effect of surface roughness, Langmuir 38 (2022) 7218–7224, https://doi.org/10.1021/acs.langmuir.2c00588.
[42] I.A. Raj, K.I. Vasu, Transition metal-based hydrogen electrodes in alkaline solution - electrocatalysis on nickel based binary alloy coatings, J. Appl. Electrochem. 20 (1990) 32–38, https://doi.org/10.1007/BF01012468.
[43] J. Zhang, T. Wang, P. Liu, Z. Liao, S. Liu, X. Zhuang, M. Chen, E. Zschech, X. Feng, Efficient hydrogen production on $MoNi_4$ electrocatalysts with fast water dissociation kinetics, Nat. Commun. 8 (2017), 15437, https://doi.org/10.1038/ncomms15437.
[44] M. Wang, H. Yang, J. Shi, Y. Chen, Y. Zhou, L. Wang, S. Di, X. Zhao, J. Zhong, T. Cheng, W. Zhou, Y. Li, Alloying nickel with molybdenum significantly accelerates alkaline hydrogen electrocatalysis, Angew. Chem. Int. Ed. 60 (2021) 5771–5777, https://doi.org/10.1002/ange.202013047.
[45] A. Nairan, P. Zou, C. Liang, J. Liu, D. Wu, P. Liu, C. Yang, NiMo solid solution nanowire array electrodes for highly efficient hydrogen evolution reaction, Adv. Funct. Mater. 29 (2019), 1903747, https://doi.org/10.1002/adfm.201903747.
[46] L. Rößner, H. Schwarz, I. Veremchuk, R. Zerdoumi, T. Seyller, M. Armbrüster, Challenging the durability of intermetallic Mo–Ni compounds in the hydrogen evolution reaction, ACS Appl. Mater. Interfaces 13 (2021) 23616–23626, https://doi.org/10.1021/acsami.1c02169.
[47] M.R.G. de Chialvo, A.C. Chialvo, Hydrogen evolution reaction on smooth $Ni_{(1-x)}$+ $Mo_{(x)}$ alloys ($0 \leq x \leq 0.25$), J. Electroanal. Chem. 448 (1998) 87–93, https://doi.org/10.1016/S0022-0728(98)00011-4.
[48] S. Battiato, L. Bruno, A. Terrasi, S. Mirabella, Superior performances of electroless-deposited Ni–P films decorated with an ultralow content of Pt for water-splitting reactions, ACS Appl. Energy Mater. 5 (2022) 2391–2399, https://doi.org/10.1021/acsaem.1c03880.
[49] M. Baek, G.-W. Kim, T. Park, K. Yong, NiMoFe and NiMoFeP as complementary electrocatalysts for efficient overall water splitting and their application in PV-electrolysis with STH 12.3, Small 15 (2019), 1905501, https://doi.org/10.1002/smll.201905501.
[50] Y. Yan, X. Cao, L. Ning, F. Lin, W. Qin, X. Liu, W. Gu, NiMo-based nanorod arrays supported on Ni foams for efficient hydrogen electrocatalysis, ACS Appl. Nano Mater. 5 (2022) 7778–7786, https://doi.org/10.1021/acsanm.2c00774.
[51] P.F. Barbieri, A. de Siervo, M.F. Carazzolle, R. Landers, G.G. Kleiman, XPS and XAES study of Ag–Pd and Cu–Ni alloys: spectra, shifts and electronic structure information, J. Electron. Spectrosc. Relat. Phenom. 135 (2004) 113–118, https://doi.org/10.1016/j.elspec.2004.02.121.
[52] C. Wei, Y. Sun, G. Scherer, A. Fisher, M. Sherburne, J. Ager, Z. Xu, Surface composition dependent ligand effect in tuning the activity of nickel-copper bimetallic electrocatalysts toward hydrogen evolution in alkaline, J. Am. Chem. Soc. 142 (2020) 7765–7775, https://doi.org/10.1021/jacs.9b12005.
[53] J. Liu, E. Tennessen, J. Miao, Y. Huang, J.M. Rondinelli, H. Heinz, Understanding chemical bonding in alloys and the representation in atomistic simulations, J. Phys. Chem. C. 122 (2018) 14996–15009, https://doi.org/10.1021/acs.jpcc.8b01891.
[54] M. Kim, J. Park, H. Ju, J.Y. Kim, H.-S. Sho, C.-H. Kim, B.-H. Kim, S.W. Lee, Understanding synergistic metal–oxide interactions of in situ exsolved metal nanoparticles on a pyrochlore oxide support for enhanced water splitting, Energy Environ. Sci. 14 (2021) 3053–3063, https://doi.org/10.1039/D0EE02935A.
[55] J.B. Mann, T.L. Meek, E.T. Knight, J.F. Capitani, L.C. Allen, Configuration energies of the d-block elements, J. Am. Chem. Soc. 122 (2000) 5132–5137, https://doi.org/10.1021/ja9928677.
[56] W. Liu, Y. Yang, L. Chen, E. Xu, J. Xu, S. Hong, X. Zhang, M. Wei, Atomically-ordered active sites in NiMo intermetallic compound toward low-pressure hydrodeoxygenation of furfural, Appl. Catal. B Environ. 282 (2021), 119569, https://doi.org/10.1016/j.apcatb.2020.119569.
[57] G. Fu, X. Kang, Y. Zhang, X. Yang, L. Wang, X.-Z. Fu, J. Zhang, J.-L. Luo, J. Liu, Coordination effect-promoted durable $Ni(OH)_2$ for energy-saving hydrogen evolution from water/methanol co-electrocatalysis, Nano-Micro Lett. 14 (2022), 200, https://doi.org/10.1007/s40820-022-00940-3.
[58] J. Song, C. Wei, Z.-F. Huang, C. Liu, L. Zeng, X. Wang, Z.J. Xu, A review on fundamentals for designing oxygen evolution electrocatalysts, Chem. Soc. Rev. 49 (2020) 2196, https://doi.org/10.1039/C9CS00607A.
[59] J. Zhao, J.-J. Zhang, Z.-Y. Li, X.-H. Bu, Recent progress on NiFe-based electrocatalysts for the oxygen evolution reaction, Small 16 (2020), 2003916, https://doi.org/10.1002/smll.202003916.
[60] J. Liu, J. Wang, B. Zhang, Y. Ruan, L. Lv, X. Ji, K. Xu, L. Miao, J. Jiang, Hierarchical $NiCo_2S_4$@NiFe LDH heterostructures supported on nickel foam for enhanced overall-water-splitting activity, ACS Appl. Mater. Interfaces 9 (2017) 15364–15372, https://doi.org/10.1021/acsami.7b00019.
[61] Q. Wang, L. Shang, R. Shi, X. Zhang, Y. Zhao, G.I.N. Waterhouse, L. Wu, C. Tung, T. Zhang, NiFe layered double hydroxide nanoparticles on Co,N-codoped carbon nanoframes as efficient bifunctional catalysts for rechargeable zinc-air batteries, Adv. Energy Mater. 7 (2017), 1700467, https://doi.org/10.1002/aenm.201700467.
[62] M. Tian, C. Liu, Z.G. Neale, J. Zheng, D. Long, G. Cao, Chemically bonding NiFe-LDH nanosheets on rGO for superior lithium-ion capacitors, ACS Appl. Mater. Interfaces 11 (2019) 35977–35986, https://doi.org/10.1021/acsami.9b10719.
[63] Y. Hou, M.R. Lohe, J. Zhang, S. Liu, X. Zhuang, X. Feng, Vertically oriented cobalt selenide/NiFe layered-double-hydroxide nanosheets supported on exfoliated graphene foil: an efficient 3D electrode for overall water splitting, Energy Environ. Sci. 9 (2016) 478–483, https://doi.org/10.1039/C5EE03440J.
[64] T. Yamashita, P. Hayes, Analysis of XPS spectra of Fe^{2+} and Fe^{3+} ions in oxide materials, Appl. Surf. Sci. 254 (2008) 2441–2449, https://doi.org/10.1016/j.apsusc.2007.09.063.
[65] L. Trotochaud, S.L. Young, J.K. Ranney, S.W. Boettcher, Nickel-iron oxyhydroxide oxygen-evolution electrocatalysts: the role of intentional and incidental iron incorporation, J. Am. Chem. Soc. 136 (2014) 6744–6753, https://doi.org/10.1021/ja502379c.
[66] L.-M. Cao, J.-W. Wang, D.-C. Zhong, T.-B. Lu, Template-directed synthesis of sulphur doped NiCoFe layered double hydroxide porous nanosheets with enhanced electrocatalytic activity for the oxygen evolution reaction, J. Mater. Chem. A 6 (2018) 3224–3230, https://doi.org/10.1039/C7TA09734D.
[67] S. Mathi, J. Jayabharathi, Enhanced stability and ultrahigh activity of amorphous ripple nanostructured Ni-doped Fe oxyhydroxide electrode toward synergetic electrocatalytic water splitting, RSC Adv. 10 (2020) 26364–26373, https://doi.org/10.1039/D0RA04828C.
[68] M.W. Louie, A.T. Bell, An investigation of thin-film Ni–Fe oxide catalysts for the electrochemical evolution of oxygen, J. Am. Chem. Soc. 135 (2013) 12329–12337, https://doi.org/10.1021/ja405351s.
[69] J. Huang, Y. Li, Y. Zhang, G. Rao, C. Wu, Y. Hu, X. Wang, R. Lu, Y. Li, J. Xiong, Identification of key reversible intermediates in self-reconstructed nickel-based hybrid electrocatalysts for oxygen evolution, Angew. Chem. Int. Ed. 58 (2019) 17458–17464, https://doi.org/10.1002/ange.201910716.
[70] K. Jiang, W. Liu, W. Lai, M. Wang, Q. Li, Z. Wang, J. Yuan, Y. Deng, J. Bao, H. Ji, NiFe layered double hydroxide/FeOOH Heterostructure nanosheets as an efficient

and durable bifunctional electrocatalyst for overall seawater splitting, Inorg. Chem. 60 (2021) 17371–17378, https://doi.org/10.1021/acs.inorgchem.1c02903.

[71] Z. Qiu, C.-W. Tai, G.A. Niklasson, T. Edivinsson, Direct observation of active catalyst surface phases and the effect of dynamic self-optimization in NiFe-layered double hydroxides for alkaline water splitting, Energy Environ. Sci. 12 (2019) 572–581, https://doi.org/10.1039/C8EE03282C.

[72] W.D. Chemelewski, H.-C. Lee, J.-F. Lin, A.J. Bard, C.B. Mullins, Amorphous FeOOH oxygen evolution reaction catalyst for photoelectrochemical water splitting, J. Am. Chem. Soc. 136 (2014) 2843–2850, https://doi.org/10.1021/ja411835a.

[73] J.-L. Ortiz-Quiñonez, U. Pal, M.S. Villanueva, Structural, magnetic, and catalytic evaluation of spinel Co, Ni, and Co-Ni ferrite nanoparticles fabricated by low-temperature solution combustion process, ACS Omega 3 (2018) 14986–15001, https://doi.org/10.1021/acsomega.8b02229.

[74] X. Bo, Y. Li, X. Chen, C. Zhao, Operando raman spectroscopy reveals Cr-induced-phase reconstruction of NiFe and CoFe oxyhydroxides for enhanced electrocatalytic water oxidation, Chem. Mater. 32 (2020) 4303–4311, https://doi.org/10.1021/acs.chemmater/0c01067.

[75] H. Shin, H. Xiao, W.A. Goddard, In silico discovery of new dopants for Fe-doped Ni oxyhydroxide ($Ni_{1-x}Fe_xOOH$) catalysts for oxygen evolution reaction, J. Am. Chem. Soc. 140 (2018) 6745–6748, https://doi.org/10.1021/jacs.8b02225.

[76] D. Friebel, M.W. Louie, M. Bajdich, K.E. Sanwald, Y. Cai, A.M. Wise, M.-J. Cheng, D. Sokaras, T.-C. Weng, R. Alonso-Mori, R.C. Davis, J.R. Bargar, J.K. Nørskov, A. Nilsson, A.T. Bell, Identification of highly active Fe sites in (Ni,Fe)OOH for electrocatalytic water splitting, J. Am. Chem. Soc. 137 (2015) 1305–1313, https://doi.org/10.1021/ja511559d.